MULTIPLE-RELAXATION-TIME LATTICE BOLTZMANN SIMULATIONS OF TURBULENT PIPE FLOWS

by

Harish Opadrishta

A thesis submitted to the Faculty of the University of Delaware in partial fulfillment of the requirements for the degree of Master of Science in Mechanical Engineering

Summer 2016

MULTIPLE-RELAXATION-TIME LATTICE BOLTZMANN SIMULATIONS OF TURBULENT PIPE FLOWS

by

Harish Opadrishta

Approved: _____

Lian-Ping Wang, Ph.D.
Professor in charge of thesis on behalf of the Advisory Committee

Approved: _____

Suresh G. Advani, Ph.D.
Chair of the Department of Mechanical Engineering

Approved: _____

Babatunde A. Ogunnaike, Ph.D.
Dean of the College of Engineering

Approved: _____

Ann L. Ardis, Ph.D.
Senior Vice Provost for Graduate and Professional Education

ACKNOWLEDGMENTS

I would like to give my sincere gratitude to my advisor, Dr. Lian-Ping Wang for his inspiring encouragement and strong support for the past two years. It is an honor for me to have the great opportunity to work with him and learn from him. None of the research work could be achieved without his rigorous training and earnest instruction.

I also want to express my gratitude to Dr. Leonard Schwartz and Dr. Suresh Advani for serving on the committee of my defense and providing many valuable comments and suggestions. I have also learned a lot of useful knowledge from the courses they offered.

From oceans apart, I would like to thank my parents for their constant blessings and well wishes. Nothing would have been possible without their emotional and financial support and I would like to dedicate this thesis to them.

I am particularly grateful to my lab mates Mr. Cheng Peng, for his help on the derivation of the $D3Q27$ model and Mr. Nick Geneva, for his help on the implementation of the model in a FORTRAN code. Many thanks to my lab mates, Mr. Sandipan Banerjee, Mr. Haoda Min, Mr. Nicolas Geneva, Ms. Xin Wen and other friends for their kind assistance and encouragement.

This work has been supported by the U.S. National Science Foundation (NSF) under the grant CBET-1235974. Thanks to the National Center for Atmospheric Research and the University of Delaware for providing the computing resources through CISL-P35751014, CISL-UDEL0001.

TABLE OF CONTENTS

LIST OF TABLES

LIST OF FIGURES

ABSTRACT

Turbulent pipe flows are encountered in a multitude of engineering applications. Some of the examples include removal of moisture, odors and other harmful gases using exhaust pipes; transporting crude oil and cooling water in oil refineries; circulation of coolants through the engine in automobiles and motorcycles; etc. They have been studied experimentally for more than a century and by direct numerical simulations (DNS) for more than two decades. Over the past twenty years, there has been an increase in the involvement of computation in studying turbulent flows, including turbulent pipe flows. The low cost and time consumption of computer simulations, along with the ability to study complex dynamic processes that are practically intractable at all scales, have resulted in the increase in their use in research. At the same time, the presence of curved boundary remains a challenge for accurate DNS of this simple flow.

In the recent past, lattice Boltzmann method (LBM) has emerged as an attractive option for simulating wall-bounded turbulent flows. It offers several advantages compared to the conventional models of computational fluid dynamics, due to the local nature of operations involved and easy implementation of boundary conditions. Despite the advantages posed by the LBM, no DNS of turbulent pipe flow has been reported using LBM. Hence, the objective of this study is to develop a lattice Boltzmann model to simulate turbulent pipe flow and implement it into a computer code using FORTRAN and MPI. This code is then used to simulate fully developed turbulent pipe flow and validate the results with the existing benchmark data.

In this thesis, the lattice Boltzmann model in three spatial dimensions using 27 mesoscopic velocities on a cubic grid was designed using an "inverse design" analysis. Yu et al.'s double interpolation scheme was used to satisfy the no-slip condition at the solid-liquid interface.

The code was first validated by simulating laminar channel and pipe flows. The profiles of streamwise velocity for the laminar pipe and channel flow simulations were observed to be in excellent agreement with the analytical results. Further, the results of the time evolution of the centerline streamwise velocity for the laminar pipe and channel flow also matched the analytical results. Hence, the validity and accuracy of the code was established.

Turbulent pipe flow was then simulated using the $D3Q27$ model. The first and second order statistics of the turbulent pipe flow simulation from the $D3Q27$, $D3Q19$ model were compared with the reference data being obtained from the spectral and finite volume discretizations of the Navier-Stokes equation. The mean velocity profiles of the $D3Q27$ simulation matched well with the reference data. On the other hand, the $D3Q19$ model under-predicts the mean velocity, especially near the center. In addition, the contours of the streamwise velocity for the $D3Q19$ simulation showed a certain preference along particular directions. This was not observed in the $D3Q27$ simulation. The erroneous results of the $D3Q19$ model could be explained by the hypothesis stated in White et al., stating that the presence of "defective planes" could be a plausible reason for the errors in the measurement of streamwise velocity in the $D3Q19$ model. Hence, the $D3Q27$ model, seems like a suitable option to simulate wall-bounded turbulent flows with a curved boundary. The only drawback to using the $D3Q27$ model, is its slower execution speed as it takes 21% more CPU time than the $D3Q19$ model.

Chapter 1

INTRODUCTION

1.1 Motivation and Objectives

Pipe flow is the flow of fluids inside a closed circular conduit and is commonly encountered in many engineering and biological processes. The water we use is distributed to our homes using a network of pipes. Blood is also transported to and from different parts of our bodies through arteries and veins. In HVAC applications, exhaust pipes are used to remove moisture, odors, carbon dioxide and other harmful gases. In oil refineries, crude oil, and cooling water are transported directly from their sources through pipes which are kilometers in length. The oil is then processed in the refinery and refined to more useful components. These components are transported from one refinery unit to another with the help of pipes. In automobiles and motorcycles, the engine temperature is maintained by circulating a coolant through the engine. This coolant is then transported to and from the radiator with the help of tubes. Further, toxic gases generated during the burning of fuel in an automobile must be completely removed with the help of exhaust pipes. These pipes must be carefully designed and maintained and any mismanagement of these pipes could result in fatal accidents. Another application where the design of pipes has a great impact is nuclear engineering. A more recent application is in the area of microfluidics, where we use pipes of diameters less than 1 mm in niche applications such as inkjet printing, gas chromatography, lab-on-a-chip and advanced drug delivery systems. The majority of the flows mentioned above are turbulent flows. Turbulent flows are characterized by random and chaotic three-dimensional vorticity. When turbulence is present, it usually dominates all other flow phenomena and results in increased energy input, viscous dissipation, mixing, heat transfer and drag. [1]

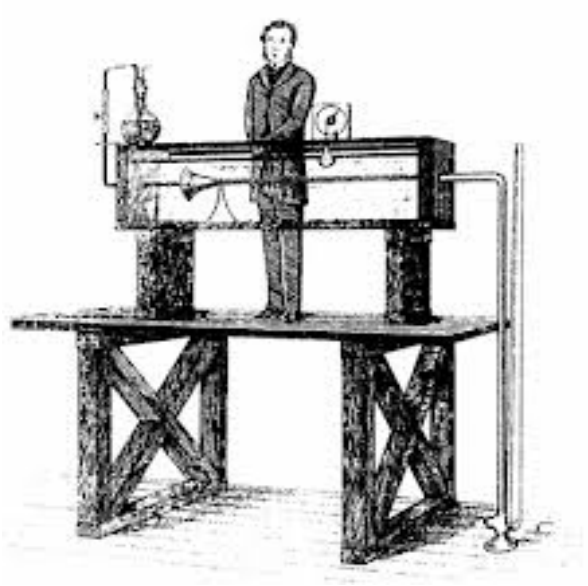

Figure 1.1: Reynolds pipe flow experiment, taken from his 1883 paper [2].

Fully developed turbulent pipe flows have been studied experimentally for more than a century and by direct numerical simulations, for more than two decades [3]. Osborne Reynolds (1883) in his path-breaking experiment visually demonstrated the transition from laminar to turbulent flows and found that below a certain critical velocity laminar flow prevails. This critical point can be expressed in terms of a dimensionless quantity known as the Reynolds number. In an attempt to determine the average flow profiles and viscous drag, Reynolds rewrote the equations of motion, separating the quantities into two parts: average and fluctuating terms. This method is known as the Reynold's decomposition and is one of the seminal concepts in studying turbulent flows [4]. Nikuradse (1933) conducted a comprehensive study of turbulent flow in pipes of varying relative roughness with Reynolds numbers ranging from $\mathrm{Re} = 10^4$ to 10^6. He also compared the velocity distributions for a given relative roughness with varying Reynolds number and remarked that the velocity profiles show a very slight dependence on the Reynolds number. Moody (1944) drew a chart comparing the friction factor against the Reynolds number and relative roughness. This chart is known as the Moody's diagram and is still one of the most widely accepted and used charts in engineering. Laufer (1954) in his report to the National Advisory Committee

for Aeronautics, gave a description of how the mean and the statistical quantities such as Reynolds stresses, turbulent dissipation, and energy spectra vary in fully developed turbulent pipe flow. Lundgren (1971) pursued an analytical treatment of steady, wall-bounded turbulent flows using the equations proposed by Prandtl. Kline (1978) in his talk at the "Workshop on coherent structure of turbulent boundary layers" emphasized the role of flow visualization in understanding complicated turbulent phenomena. Three years later, Carlson et al. used flow visualization techniques to study the transition from laminar to turbulent in a plane Poiseulle flow. Tu and Ramaprian (1983) conducted an experimental investigation of periodic turbulent pipe flow and compared these results with numerical calculations using a quasi-steady turbulence closure model. Reich (1989) studied the effect of rotation on the velocity and temperature distribution in a turbulent pipe flow. During the last two decades, owing to the growth in computational capabilities, numerical simulations of turbulent flows have become an important research tool in studying the basic physics of turbulence [11]. In 1991, Eggels presented his work on Large-eddy simulation of turbulent pipe flow at the 1st European Fluid Mechanics conference in Cambridge, United Kingdom. Two years later, Eggels et al. performed the first Direct Numerical Simulation(DNS) of pipe flow in which they simulated fully developed turbulent flow using a finite volume discretization of the Navier-Stokes equation by resolving all scales of motion. The agreement between the simulation data and experimental data was reasonable for turbulence statistics up to fourth order.

In the last two decades, there has been a renewed interest in studying wall-bounded turbulence stimulated by some controversial results. Barenblatt et al. (1997) suggested that the velocity profile in the intermediate region of the turbulent pipe, flow obeys a power law rather than the von Karman-Prandtl log law. By contrast, George and coworkers have suggested that the overlap velocity profiles and friction law for boundary layers are power laws, however, the corresponding relations for pipes and channels are logarithmic [1]. The study from the superpipe experiment conducted by Zagarola and Smits (1998) states that the mean velocity profile in the overlap region is

given by the power law for small Reynolds number. However, as the Reynolds number increases to greater than 400×10^3, another overlap region is apparent and the mean velocity profile in this region is described by the log-law. Xu et al. (2004) formulated a compressible finite volume model based on the Navier-Stokes equation for large eddy simulation of compressible turbulent pipe flows at low Mach number. Peixinho and Mullin (2006) worked on the decay of turbulence in pipe flow. They devised a novel experiment in which they decreased the turbulence by reducing Reynolds number and observed how the disordered motion decayed.

Over the last ten years, several groups have been working hard to make breakthroughs in understanding the fundamental problem posed by Prof. Reynolds i.e. turbulent transition in pipe flow. Eckhardt and colleagues stated that the features of turbulence can be accounted by assuming that the turbulent state corresponds to a chaotic saddle. Wu and colleagues focused on the direct numerical simulations of turbulent pipe flow. In an article to the "Proceedings of the National Academy of Sciences in the United States of America", Wu et al. tried to understand the dynamics behind the pipe transition by developing a direct simulation of the gradual transition to the turbulent state as opposed to an abrupt transition. They achieved this by a weak but a finite perturbation of the laminar flow. Bailey et al. (2014) tried to find an estimate for von Karman's constant in turbulent pipe flow by conducting experiments in the Princeton/ONR superpipe. Finally, Chin et al. (2015) tried to provide a comparison between numerical simulations and experiment. They tried to compare LES, DNS and hot-wire experiment data for a turbulent pipe flow with friction Reynold's number equal to 1000 and observed that the turbulence statistics showed good agreement up to the fourth order.

In the studies mentioned above, one can notice the increasing involvement of computation in turbulence research over the last twenty years. Computational fluid dynamics (CFD) is developing into a powerful tool capable of simulating turbulent flows directly, resulting in a database which gives us a complete solution of flow field across the whole domain. The development has been so rapid that CFD is now used as

much as the traditional didactic and research methods of experimentation and analytical modeling to solve fluid flow problems. This recent adoption of CFD has been both inevitable and progressive, as the high costs and time consumption associated with experimentation has often precluded the desire to produce efficient in-depth results. In addition, experiments cannot be used to study complex processes that are practically intractable. Moreover, the assumptions, generalizations, and approximations associated with analytical models have swayed their reduction in the development of flow solutions. By considering these limitations coupled with recent achievements in the development of numerical solutions for the Navier-Stokes equations and the amelioration of computing power and efficiency, it is easy to understand why confidence has both increased and advanced the application of CFD as a viable alternative in industry and science [18].

The traditional approach for computational treatment of fluid flows consists of solving the Navier-Stokes and the continuity equation using numerical analysis and computer algorithms. In recent years, the lattice Boltzmann method (LBM) has developed into an alternate and promising computational tool for simulating fluid flows and modeling physics in fluids [19].

LBM is a mesoscopic method based on solving the Boltzmann equation governing the distribution of fluid-particle velocity at the given location and time. The following are the advantages LBM offers as compared to the conventional models of CFD:

1. It is conveniently easy and straightforward to derive LBM models for fluid flow and implement these models in numerical algorithms.

2. Modeling of multi-phase flows and flows in complex boundaries are relatively simple due to easy implementation of boundary conditions.

3. Pressure is calculated using an equation of state as opposed to solving the Poisson equation for the incompressible Navier-Stokes equation. This eliminates the numerical challenges which require special treatments, such as iteration or relaxation.

4. The local nature of the operations involved in LBM makes the method very

easy to implement in parallel computer systems.

5. In small-scale flows where the continuity approximation in the Navier-Stokes equation does not hold, LBM with some modifications could still work.

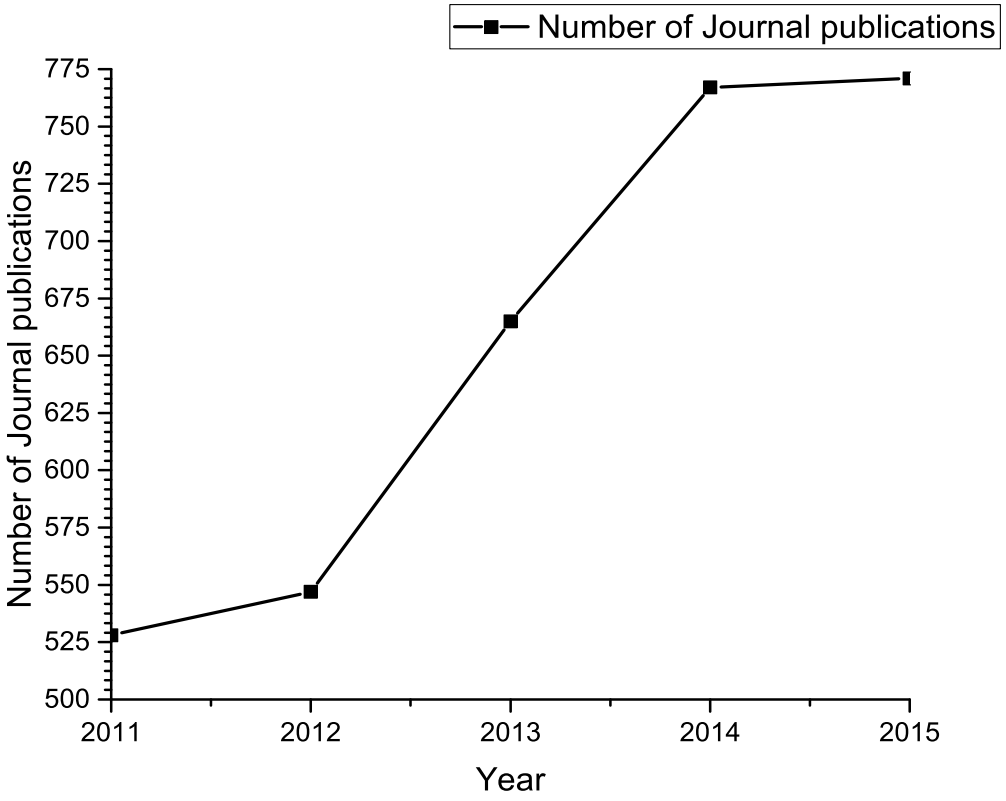

Figure 1.2: Number of journal publications vs the year published. Information obtained from "Web of Science".

From the reasons mentioned above, LBM is fast emerging as an attractive method for CFD. This is demonstrated in Fig. 2, where we can see how the number of journal publications in LBM has increased over time. In spite of these advantages, it is fraught with stability issues and has difficulties in simulating high Reynolds number flows. These are some of the challenges we have come across while simulating turbulent pipe flow using LBM.

Turbulent flows are characterized by a wide range of length and time scales. This has been the reason for their innate complexity and has inspired remarks ranging

from Lamb's "chief outstanding difficulty of our subject" to Bradshaw's more cynical "invention of the Devil on the seventh day of creation". One way to model these flows is by spatially filtering the smaller scales of motion and then solving for the others. The effects of the smaller scales of motion are then approximated by a model. This method is known as large eddy simulation (LES) and is widely used to simulate turbulent flows using LBM. An alternative method involves resolving all length scales including the Kolmogorov's length scale (smallest scale of motion in turbulent flow) and solving numerically for the velocity and pressure as a function of space and time. These numerical solutions are termed direct numerical simulations (DNS) . The first DNS was performed in 1972 at the National Center for Atmospheric Research by Orszag & Patterson. They performed a 32^3 computation of isotropic turbulence at a Reynolds number (based on Taylor micro scale) of 35. However, it wasn't until 1987 that the DNS of wall-bounded turbulent flow was first performed by Kim et al., using the spectral method [20].

One of the major disadvantages of performing DNS is the computational cost involved. This restricts the application of DNS to low Reynolds number flows. For example, in order to simulate what happens inside the atmospheric planetary boundary layer (PBL), you need to model length scales on the order of millimeters to length scales on the order of kilometers; the entire scale range spans more than six orders of magnitude. Hence, DNS of a turbulent required at least 10^{18} numerical grid points. To put this into perspective, the DNS performed in this thesis used approximately 5.4×10^7 grid points and the largest DNS performed today uses approximately 10^{10} grid points. This is far beyond today's computing capacity or that in the foreseeable future [22].

In spite of this, there is a myriad of advantages and applications involved with DNS. Some of these include [20]:

1. The most important contribution of DNS has been in phenomenological modeling for engineering applications. Several terms needed for the Reynolds stress

equations, which form the basis for closure of the Reynolds averaged mean flow equations, contain several terms that must be modeled but are difficult to measure experimentally. However, in DNS, all the terms in the Reynolds stress equations can be directly computed.

2. DNS simulations possess the highest degree of exactness in the data. This attribute of DNS helped us provide a more realistic view of the structure of turbulent boundary layer. Instead of predicting experimentally measured statistical correlations, DNS can be used to yield information that may be impossible to obtain from experiments. The confidence in DNS data has progressed to the point where modern ideas on coherent structures of turbulence are routinely evaluated using DNS data.

Hence, DNS can be viewed as a numerical experiment producing a series of non-empirical solutions, from first principles, for a virtual or realistic turbulent flow. Its great strength is the ability to provide complete knowledge, unaffected by approximations, at all points within the flow, at all times within the simulation period.

From the information stated above, it is desirable to develop new and alternative DNS methods to study turbulent pipe flow. The lattice Boltzmann method seemed to be an apt choice for this purpose due to the parallel nature of its algorithm. However, according to the best of the author's knowledge, no DNS of turbulent pipe flow has been reported using LBM. The difficulty might be the treatment of curved wall using a structured lattice grid. Hence, the objective of this study is to develop a lattice Boltzmann model to simulate turbulent pipe flow and to incorporate it into a numerical tool using FORTRAN and MPI. The final goal of this study is to simulate turbulent pipe flow and validate the results with the existing benchmark data.

1.2 Outline of the Thesis

In Chapter 2 we present a brief introduction of LBM, i.e. a description of the Boltzmann equation and a derivation of the lattice Boltzmann equation. We discuss the different types of LBM collision models: the Bhatnagar-Gross-Krook model and the multi-relaxation-time model [21]. Next, we describe the 3 common lattices that are

used in the 3D simulation of turbulent flows: $D3Q15, D3Q19$, and the $D3Q27$ lattice. We end the chapter by discussing the many applications of the lattice Boltzmann method over the last 20 years.

In Chapter 3, we derive the model used to simulate turbulent pipe flow. We also provide a brief description of the boundary conditions used for the simulation. We end the chapter by explaining the algorithm used for implementing the LBM model in a FORTRAN code.

In Chapter 4 we validate the code by comparing laminar channel and pipe flow simulation results with the analytical results and compare the performance of two LBM models with each other and with the benchmark, for laminar and turbulent pipe flow simulations. Chapter 5 starts with a discussion of the results obtained and culminates by stating the conclusion of the study.

Chapter 2

THEORETICAL BACKGROUND: THE LATTICE BOLTZMANN METHOD

2.1 The Boltzmann Equation

A statistical description of a fluid system is given by the quantity $f(\mathbf{r}, \mathbf{c}, t)$, otherwise known as the particle or molecular distribution function. The distribution function describes the number of molecules at time t positioned between $\mathbf{r}$ and $\mathbf{r} + d\mathbf{r}$ which have velocities between $\mathbf{c}$ and $\mathbf{c} + d\mathbf{c}$. The distribution function is governed by:

$$\frac{\partial f}{\partial t} + \frac{\partial f}{\partial \mathbf{r}} \cdot \mathbf{c} + \frac{\mathbf{F}}{m} \cdot \frac{\partial f}{\partial \mathbf{c}} = \Omega \tag{2.1}$$

where Ω is the collision term representing the effects of molecular interactions, $\mathbf{F}$ is the external force applied and m is the mass of the particle [23].

The above equation is known as the Boltzmann equation and was established by Ludwig Boltzmann in 1872. It is the cornerstone of "kinetic theory", which is a branch of statistical mechanics dealing with dyamics of non-equilibrium processes and their relaxation to thermodynamic equilibrium.

If the external force applied is zero, then Eq. (2.1) becomes:

$$\frac{\partial f}{\partial t} + \mathbf{c} \cdot \nabla f = \Omega \tag{2.2}$$

The L.H.S in the above equation represents the change in the number of molecules due to advection and the R.H.S represents the change in the number of molecules due to collisions. The relation between the above equation and the macroscopic quantities such as fluid density ρ, fluid velocity vector $\mathbf{u}$, and internal energy e, is as follows:

$$\rho(\mathbf{r}, t) = \int m f(\mathbf{r}, \mathbf{c}, t) d\mathbf{c} \tag{2.3}$$

$$\rho(\mathbf{r},t)\mathbf{u}(\mathbf{r},t) = \int m\mathbf{c}f(\mathbf{r},\mathbf{c},t)d\mathbf{c} \tag{2.4}$$

$$\rho(\mathbf{r},t)e(\mathbf{r},t) = \frac{1}{2}\int mu_a^2 f(\mathbf{r},\mathbf{c},t)dc \tag{2.5}$$

where u_a is the velocity of the particle relative to the fluid.

2.2 From the Boltzmann Equation to the Lattice Boltzmann Equation

The lattice Boltzmann equation is a discretized form of the continuous Boltzmann equation. The Boltzmann equation can be expressed in the following form:

$$\left(\frac{\partial}{\partial t} + \mathbf{c}\cdot\nabla\right)f = \Omega \tag{2.6}$$

According to the Bhatnagar-Gross-Krook approximation, the collision term can be expressed as [25]:

$$\Omega = \frac{1}{\tau}(f^{eq} - f) \tag{2.7}$$

where τ is the relaxation parameter, the rate at which the system relaxes to equilibrium and f^{eq} is the particle distribution function at equilibrium. Eq. (2.6) can then be integrated with respect to time

$$\int\left(\left(\frac{\partial}{\partial t} + \mathbf{c}\cdot\nabla\right)f\right)dt = \int\left(\frac{1}{\tau}(f^{eq} - f)\right)dt \tag{2.8}$$

Applying the trapezoidal rule of integration, we have:

$$f(\mathbf{r}+\mathbf{c}\Delta t, t+\Delta t) - f(\mathbf{r},t) = -\frac{\Delta t}{2\tau}(f(\mathbf{r}+\mathbf{c}\Delta t, t+\Delta t) - f^{(eq)}(t+\Delta t)) - \frac{\Delta t}{2\tau}(f(\mathbf{r},t) - f^{(eq)}(t)) \tag{2.9}$$

where Δt is the value of time increment. Rearranging the above equation and redefining the particle distribution function, we have:

$$\overline{f}(\mathbf{r}+\mathbf{c}\Delta t, t+\Delta t) = \overline{f}(\mathbf{r},t) + \frac{1}{\frac{1}{2}+\frac{\tau}{\Delta t}}(\overline{f}^{(eq)}(t) - \overline{f}(\mathbf{r},t)) \tag{2.10}$$

When we further discretize the above equation in velocity space, we get the final form of lattice Boltzmann equation based on the BGK approximation as:

$$\overline{f}_i(\mathbf{r}+\mathbf{c}\Delta t, t+\Delta t) - \overline{f}_i(\mathbf{r},t) = \frac{1}{\frac{1}{2}+\frac{\tau}{\Delta t}}(\overline{f}_i^{(eq)}(t) - \overline{f}_i(\mathbf{r},t)) \tag{2.11}$$

where i represents a particular direction. We can further simplify Eq. 2.11 into

$$\overline{f}_i(\mathbf{r}+\mathbf{c}\Delta t, t+\Delta t) - \overline{f}_i(\mathbf{r},t) = \frac{1}{\tau_{LBM}}(\overline{f}_i^{(eq)}(t) - \overline{f}_i(\mathbf{r},t)) \tag{2.12}$$

where $\tau_{LBM} = \frac{1}{2} + \frac{\tau}{\Delta t}$.

2.3 Theory of the Lattice Boltzmann Method

The lattice Boltzmann method which incorporates Eq. (2.11) as its governing equation, can be viewed as a special finite difference scheme for the kinetic equation of the discrete-velocity distribution function. The fundamental idea of the LBM is to construct simplified kinetic models that incorporate the essential physics of microscopic or mesoscopic processes so that the macroscopic averaged properties obey the desired macroscopic equations. The assumption one has to make for using these simplified kinetic-type methods for simulating macroscopic flows is that the collective behavior of many microscopic particles in the system is not sensitive to the underlying details in microscopic physics [24].

The key steps in the lattice Boltzmann method are streaming and collision, which are represented by the LHS and RHS of the lattice Boltzmann equation. Figure 2.1 shows graphically how the streaming step takes place for the interior nodes [19].

The collision step has already been described in the previous section. Hence, to design a lattice Boltzmann model based on the BGK approximation, one has to state the following:

1. Initialize the distribution functions.

2. The relaxation parameter which is related to the viscosity as:

$$\tau_{LBM} = \frac{1}{2}\left(6\nu\frac{\Delta t}{(\Delta x)^2} + 1\right) \tag{2.13}$$

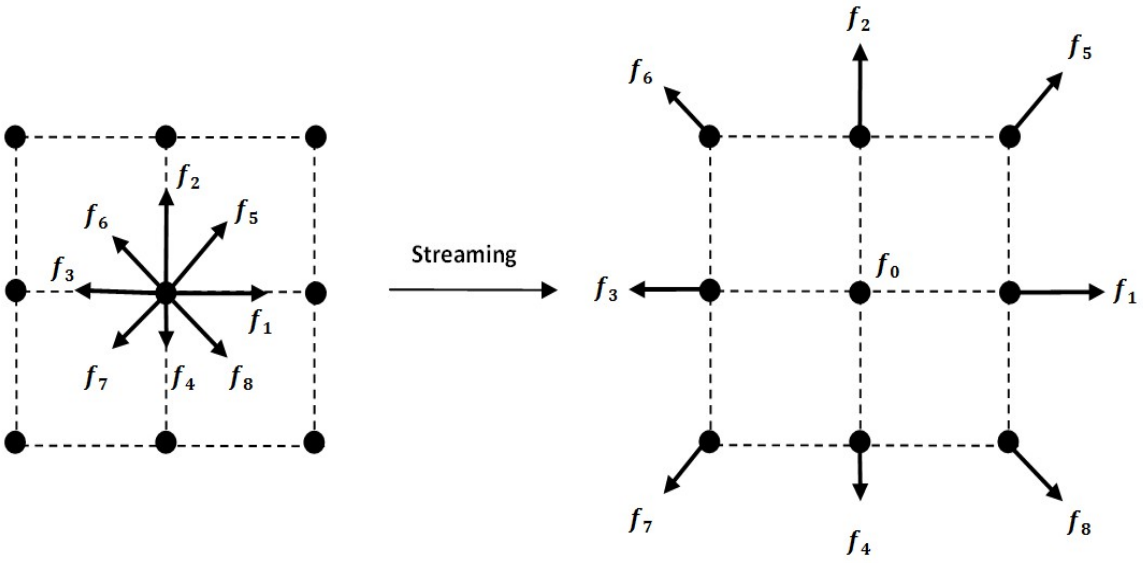

Figure 2.1: Illustration of the streaming process of a lattice node

3. The equilibrium distibution functions which is given by the equation:

$$f_i^{eq} = \omega_i \rho \left[1 + 3(c_i \cdot u) + \frac{9}{2}(c_i \cdot u)^2 - \frac{3}{2}u^2 \right] \tag{2.14}$$

Eq. (2.11), otherwise known as the lattice BGK equation, is the simplest lattice Boltzmann equation (LBE) and is based on a single-relaxation-time approximation. Due to its extreme simplicity, the lattice BGK equation has become the most popular lattice Boltzmann model. Another lattice Boltzmann model which was developed at the same time is the multiple-relaxation-time (MRT) lattice Boltzmann equation. The MRT lattice Boltzmann equation, also known as the generalized lattice Boltzmann equation (GLBE) or the moment method helps rectify some defects of the LBGK model, such as fixed Prandtl number (Pr = 1 for the BGK model) which is equal to the ratio of kinematic viscosity over thermal diffusivity, and fixed ratio between the kinematic and bulk viscosities. Though the MRT LBE schemes are slower than their BGK counterparts, they are numerically more stable [21]. As its name suggests, the multi-relaxation-time scheme consists of multiple relaxation times for different moments that may be independently adjusted. In the MRT scheme the discrete velocity vectors are converted into an equal number of moments with the help of an orthogonal

transformation matrix $\mathbf{M}$. The collision step is then performed in the moment space instead of the velocity space. The final form of the MRT LBE is:

$$f_i(r + c_i\Delta t, t + \Delta t) - f_i(r, t) = -\mathbf{M^{-1}}\hat{\mathbf{S}}\mathbf{M}((f_i(r, t) - f_i^{eq}(r, t)) \tag{2.15}$$

where $\hat{\mathbf{S}}$ is a diagonal matrix ($\hat{\mathbf{S}} \equiv diag(s_0, s_1, ..., s_N)$), consisting of the relaxation parameters. It is known as the relaxation matrix

2.4 Different Lattices used in 3D LBM

The most important component of the lattice Boltzmann method is a discrete phase space defined by a regular lattice in D dimensions and each lattice node is connected to its neighbors with a set of N discrete velocity vectors. The most commonly used lattices in 3 dimensions are discussed next.

2.4.1 D3Q15

The lattice used in the $D3Q15$ model is shown in Fig. 2.2. The discrete velocities

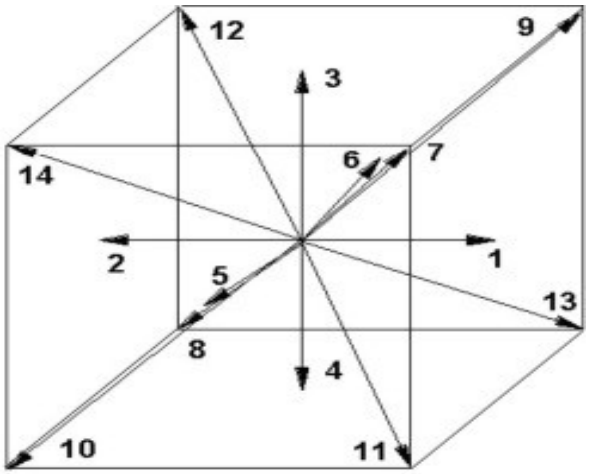

Figure 2.2: D3Q15 lattice

of the $D3Q15$ model can be expressed as:

$$c_i = \begin{cases} (0,0,0), i = 0; \\ c(\pm 1,0,0), c(0,\pm 1,0), c(0,0,\pm 1), i = 1,2,.....,6; \\ c(\pm 1,\pm 1,\pm 1), i = 7,8,.....,14 \end{cases}$$

and the lattice weights are

$$w_i = \begin{cases} 2/9, i = 0; \\ 1/9, i = 1, 2, ..., 6; \\ 1/72, i = 7, 8, ..., 14 \end{cases}$$

2.4.2 D3Q19

The lattice used in the $D3Q19$ model is shown in Fig. 2.3. The discrete velocities

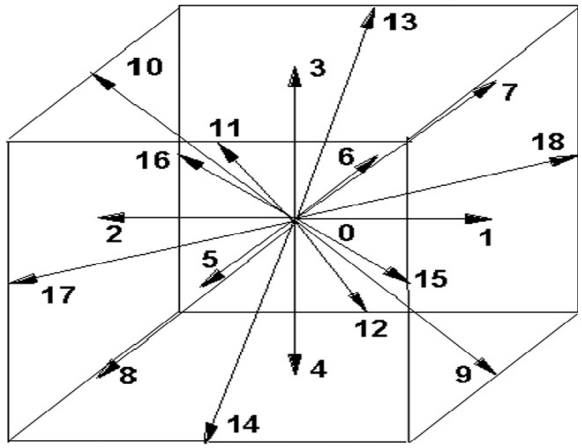

Figure 2.3: D3Q19 lattice

of the $D3Q19$ model can be expressed as:

$$c_i = \begin{cases} (0,0,0), i = 0; \\ c(\pm 1,0,0), c(0,\pm 1,0), c(0,0,\pm 1), i = 1, 2, ..., 6; \\ c(\pm 1,\pm 1,0), c(\pm 1,0,\pm 1), c(0,\pm 1,\pm 1), i = 7, 8, ..., 18 \end{cases}$$

and the lattice weights are

$$w_i = \begin{cases} 2/9, i = 0; \\ 1/18, i = 1, 2, ..., 6; \\ 1/36, i = 7, 8, ..., 14 \end{cases}$$

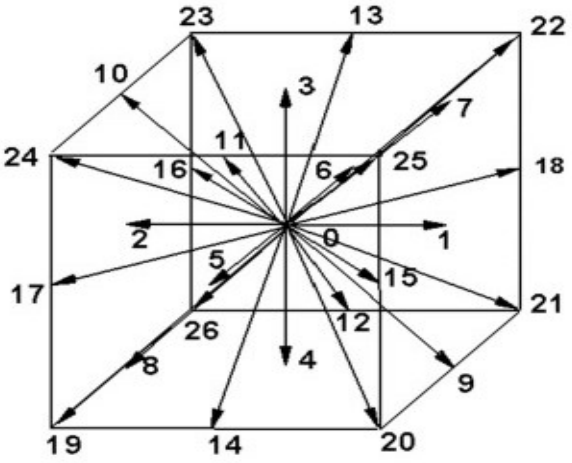

Figure 2.4: D3Q27 lattice

2.4.3 D3Q27

The lattice used in the $D3Q27$ model is shown in Fig. 2.4. The discrete velocities of the $D3Q27$ model can be expressed as:

$$c_i = \begin{cases} (0,0,0), i = 0; \\ c(\pm 1,0,0), c(0,\pm 1,0), c(0,0,\pm 1), i = 1,2,.....,6; \\ c(\pm 1,\pm 1,0), c(\pm 1,0,\pm 1), c(0,\pm 1,\pm 1), i = 7,8,.....,18; \\ c(\pm 1,\pm 1,\pm 1), i = 19,20,.....26 \end{cases}$$

and the lattice weights are

$$w_i = \begin{cases} 8/27, i = 0; \\ 2/27, i = 1,2,....,6; \\ 1/54, i = 7,8,....,18; \\ 1/216, i = 19,20,...,26 \end{cases}$$

2.5 LBM Simulations of Wall-Bounded Turbulent Flows

In recent years, several simulations of wall-bounded turbulent flows using LBM have been performed. Most researchers have used the DNS or LES models to simulate

turbulence as the turbulence model based on Reynolds-averaged-Navier-Stokes equation is not a predictive tool by itself for turbulence, but relies on empirical closure models. Lammers et al. (2005) performed the DNS of a turbulent channel flow of friction Reynolds number 180, using the D3Q19 LBGK model. For the channel flow, friction Reynolds number is calculated by using the friction velocity and the half channel width as the velocity scale and the length scale respectively. The results obtained from the DNS were compared with two data sets of a Chebhyshev psuedo-spectral method with high-quality LDA laboratory measurement data used as a benchmark. The results show that the lattice Boltzmann method produced lower-order statistics of the same quality for comparable resolution. However, neither of the computational models could produce reliable results with respect to the higher-order statistics, most notably, the flatness of the normal velocity. The study thus shows that for the case of turbulence statistics, the lattice Boltzmann codes are as reliable as the Chebyshev pseudo-spectral codes. However, the lattice Boltzmann methods have lower comparable computational cost as compared to the pseudo-spectral methods. Premnath et al. (2009) performed large eddy simulation of a turbulent channel flow of friction Reynolds number equal to 183.6 using a generalized lattice Boltzmann equation. They found that the MRT model offered better solution fidelity as opposed to the BGK model which exhibited spurious effects on velocity fluctuations in the near-wall region. Bespalko et al. (2010) performed DNS of turbulent channel flow using a $D3Q19$ MRT-LBE. Freitas et al. (2011) compared the performance of BGK, MRT and the cascaded lattice Boltzmann methods while simulating wall-bounded turbulent flows. They concluded that based on stability, advanced moment based schemes like the cascaded lattice Boltzmann model and the multi-relaxation-time model are not necessarily better than the BGK model for wall-bounded turbulent flows. Kang and Hassan (2013) investigated the effect of lattice models on the simulation results of wall-bounded turbulent flows in a circular pipe and in a square duct using LES turbulence models. They had discovered that the $D3Q19$ model produced poor results compared to that of the $D3Q27$ model and could not achieve the rotational invariance while the $D3Q27$ lattice model could. The

poor results of the $D3Q19$ model were attributed to the defective 2-D planes with five velocities, based on White and Chong's [31] hypothesis. The defective planes are better visualized in Fig. 2.5.

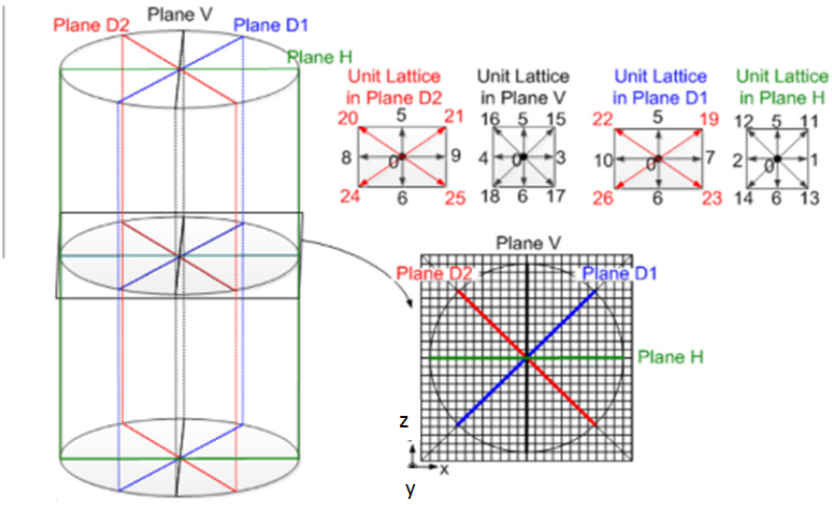

Figure 2.5: Definition of different planes associated with the pipe flow and unit lattices on these planes. Source: [30]

From Fig. 2.5, we can observe the primary difference between a $D3Q19$ and a $D3Q27$ model. The $D3Q19$ model only has five velocity vectors on diagonal planes D1 and D2, while the $D3Q27$ model has nine velocity vectors. Hence, the D1 and D2 planes can be viewed as defective planes for the $D3Q19$ model.

Suga and Kuwata (2015) performed direct numerical simulation of turbulent channel flow using a $D3Q27$ LBM model and confirmed that the method is as reliable as the spectral method when the resolution of the LBM simulation is approximately two times the resolution of the spectral simulation. In addition, they also performed large eddy simulations of pipe and porous medium flows. They concluded that the results produced by the $D3Q27$ model for simulating turbulent flows bounded by curved walls are of satisfactory accuracy, which is not the case for the $D3Q19$ model. The important features of the literature reviewed are summarized as follows:

Table 2.1: Summary of the literature reviewed in this section

Reference	Nature of simulation	LBM model	Reynolds number	Resolution
Lammers et al. [26]	DNS	$D3Q19$	180	16H $\times$ 2H $\times$ H
Premnath et al. [27]	LES	$D3Q19$	183.6	6H $\times$ 3H $\times$ H
Bespalko et al. [28]	DNS	$D3Q19$	180	12H $\times$ H $\times$ 2H
Freitas et al. [29]	DNS	$D3Q19$, $D3Q27$	200	πH $\times$ 2H $\times$ 0.289πH
Kang et al. [30]	LES	$D3Q19$, $D3Q27$	360	5D(Pipe length), H $\times$ H $\times$ 6H
Suga et al. [32]	DNS, LES	$D3Q27$	180, 360	2π H $\times$ H $\times$ π H, 400 $\times$ 75 $\times$ 75

Chapter 3

NUMERICAL METHOD

3.1 D3Q27 Lattice Boltzmann Model

In this section, we design an MRT LBM model in three spatial dimensions using 27 mesoscopic velocities (also known as $D3Q27$ model) on a cubic grid that is fully consistent with the Navier-Stokes equations with a body force term. In Section 2.3, we mentioned the components needed to design an LBGK model. In [33], Anupindi et al. use a $D3Q27$ BGK model to simulate three-dimensional lid driven flow in cubic and cuboidal cavities. Turbulence modelling in this case is performed using large eddy simulations. The steady-oscillatory transition Reynolds number in cubic and cuboidal lid-driven cavities was determined for Reynolds numbers ranging from 2100 to 2350. A mesh size of 80^3 was employed for the cubic case and $80 \times 160 \times 80$ for the cuboidal case. The values obtained for steady–oscillatory transition lie in the range of 10 - 17% to the benchmark values obtained from Navier-Stokes based simulations and experimentally measured results.

The turbulent pipe flow problem studied in this thesis has a maximum Reynolds number in the range of 3500 - 4000. Hence, we adopt a $D3Q27$ MRT model to simulate the turbulent pipe flow as it has been stated in Sec. 2.3 that MRT models exhibit greater numerical stability than their BGK counterparts. To design an MRT model, we need to specify the following components:

1. A set of moments corresponding to the discrete velocities in the model and namely, construct a transformation matrix $\mathbf{M}$ that converts the distribution functions into moments.

$$\mathbf{m} = \mathbf{M}\mathbf{f} \tag{3.1}$$

2. A set of independent relaxation parameters, which physically signify the rates at which the thermodynamic quantities reach the equilibrium state. By tuning the free relaxation parameters using sensitivity analysis, we can improve the stability of the MRT-LBM [34].

3. The values of moments at equilibrium.

4. The mesoscopic formulation of the forcing term, as well as the effect of forcing on other model details.

Let us begin with our endeavor of designing a $D3Q27$ lattice Boltzmann model for simulating fluid flow. We denote, the 27 moments of the $D3Q27$ model as:

$$\begin{aligned}\mathbf{m} = (&\delta\rho, j_x, j_y, j_z, e, p_{xx}, p_{zz}, p_{xy}, p_{yz}, p_{xz}, q_x, q_y, q_z, \pi_x,\\ &\pi_y, \pi_z, \phi_{xyz}, \epsilon, \psi_{xx}, \psi_{zz}, \psi_{xy}, \psi_{yz}, \psi_{xz}, \xi_x, \xi_y, \xi_z, e^3)\end{aligned} \tag{3.2}$$

where $\delta\rho$ is the zeroth-order moment representing local density fluctuation, $\delta\rho = \rho - \rho_0$ (ρ and ρ_0 are the density and the average density respectively); j_x, j_y, j_z are first-order moments related to the momentum in the x,y and z-directions, respectively; e is a second-order moment related to the energy; p_{xx}, p_{zz} are two second-order moments corresponding to the normal stress components; p_{xy}, p_{yz}, p_{xz} are three more second-order moments related to the shear-stress components; q_x, q_y, q_z are the third-order moments and related to the energy flux in the x, y and z-directions, respectively; π_x, π_y, π_z are three third-order moments which are related to the flux of the corresponding normal stresses in x, y and z directions; ϕ_{xyz} is an antisymmetric third-order moment related to the flux of the shear stress; ϵ is a fourth-order moment which is physically interpreted as the square of the kinetic energy; ψ_{xx}, ψ_{zz} are fourth-order moments which are related to the product of the normal stress with the energy; ψ_{xy}, ψ_{xz}, ψ_{yz} are more fourth-order moments which are related to the product of shear stresses with the energy term; ξ_x, ξ_y, ξ_z are fifth-order moments related to the flux of the energy-squared term; e^3 is a sixth-order moment which is related to the cube of the energy. To summarize, the $D3Q27$ model that we have proposed consists of one zeroth-order moment ($\delta\rho$), three first-order moments (j_x, j_y and j_z), six second-order moments (e,

p_{xx}, p_{zz}, p_{xy}, p_{xz} and p_{yz}), seven third-order moments (q_x, q_y, q_z, π_x, π_y, π_z and ϕ_{xyz}), six fourth-order moments (ϵ, ψ_{xx}, ψ_{zz}, ψ_{xy}, ψ_{xz} and ψ_{yz}), three fifth-order moments (ξ_x, ξ_y and ξ_z) and one sixth-order moment (e^3).

Through the "inverse" design analysis, we will show later that all the moments of third-order or below can be uniquely determined while the moments of order greater than three are irrelevant to the Navier-Stokes equations, and thus can be chosen somewhat freely. We construct their vectors by first exhausting all the lower order moments i.e. the zeroth, first and second order. We then construct the higher order moments based on the principle that they are independent of the lower order moments which are already constructed:

$$|\delta\rho\rangle = |e_\alpha|^0 \tag{3.3a}$$

$$|j_x\rangle = e_{\alpha x}, |j_y\rangle = e_{\alpha y}, |j_z\rangle = e_{\alpha z} \tag{3.3b}$$

$$|e\rangle = e_{\alpha x}^2 + e_{\alpha y}^2 + e_{\alpha z}^2 \tag{3.3c}$$

$$|p_{xx}\rangle = 2e_{\alpha x}^2 - e_{\alpha y}^2 - e_{\alpha z}^2 \tag{3.3d}$$

$$|p_{zz}\rangle = e_{\alpha y}^2 - e_{\alpha z}^2 \tag{3.3e}$$

$$|p_{xy}\rangle = e_{\alpha x}e_{\alpha y} \tag{3.3f}$$

$$|p_{yz}\rangle = e_{\alpha y}e_{\alpha z} \tag{3.3g}$$

$$|p_{xz}\rangle = e_{\alpha x}e_{\alpha z} \tag{3.3h}$$

$$|q_x\rangle = (e_{\alpha x}^2 + e_{\alpha y}^2 + e_{\alpha z}^2)e_{\alpha x} \tag{3.3i}$$

$$|q_y\rangle = (e_{\alpha x}^2 + e_{\alpha y}^2 + e_{\alpha z}^2)e_{\alpha y} \tag{3.3j}$$

$$|q_z\rangle = (e_{\alpha x}^2 + e_{\alpha y}^2 + e_{\alpha z}^2)e_{\alpha z} \tag{3.3k}$$

$$|\pi_x\rangle = (e_{\alpha y}^2 - e_{\alpha z}^2)e_{\alpha x} \tag{3.3l}$$

$$|\pi_y\rangle = (e_{\alpha z}^2 - e_{\alpha x}^2)e_{\alpha y} \tag{3.3m}$$

$$|\pi_z\rangle = (e_{\alpha x}^2 - e_{\alpha y}^2)e_{\alpha z} \tag{3.3n}$$

$$|\phi_{xyz}\rangle = e_{\alpha x}e_{\alpha y}e_{\alpha z} \tag{3.3o}$$

$$|\epsilon\rangle = (e_{\alpha x}^2 + e_{\alpha y}^2 + e_{\alpha z}^2)^2 \tag{3.3p}$$

$$|\psi_{xx}\rangle = (2e_{\alpha x}^2 - e_{\alpha y}^2 - e_{\alpha z}^2)(e_{\alpha x}^2 + e_{\alpha y}^2 + e_{\alpha z}^2) \tag{3.3q}$$

$$|\psi_{zz}\rangle = (e_{\alpha y}^2 - e_{\alpha z}^2)(e_{\alpha x}^2 + e_{\alpha y}^2 + e_{\alpha z}^2) \tag{3.3r}$$

$$|\psi_{xy}\rangle = e_{\alpha x}e_{\alpha y}(e_{\alpha x}^2 + e_{\alpha y}^2 + e_{\alpha z}^2) \tag{3.3s}$$

$$|\psi_{yz}\rangle = e_{\alpha y}e_{\alpha z}(e_{\alpha x}^2 + e_{\alpha y}^2 + e_{\alpha z}^2) \tag{3.3t}$$

$$|\psi_{xz}\rangle = e_{\alpha x}e_{\alpha z}(e_{\alpha x}^2 + e_{\alpha y}^2 + e_{\alpha z}^2) \tag{3.3u}$$

$$|\xi_x\rangle = (e_{\alpha x}^2 + e_{\alpha y}^2 + e_{\alpha z}^2)^2 e_{\alpha x} \tag{3.3v}$$

$$|\xi_y\rangle = (e_{\alpha x}^2 + e_{\alpha y}^2 + e_{\alpha z}^2)^2 e_{\alpha y} \tag{3.3w}$$

$$|\xi_z\rangle = (e_{\alpha x}^2 + e_{\alpha y}^2 + e_{\alpha z}^2)^2 e_{\alpha z} \tag{3.3x}$$

$$|e^3\rangle = (e_{\alpha x}^2 + e_{\alpha y}^2 + e_{\alpha z}^2)^3 \tag{3.3y}$$

where α is the index of the velocity vector from 0 to 26. The transformation matrix $\mathbf{M}$ is constructed from the above mentioned moment vectors as shown in Eq. (3.5).

The diagonal relaxation matrix $\mathbf{S}$ specifies all the relaxation parameters

$$\begin{aligned}\mathbf{S} = diag(&s_\rho, s_{j_x}, , s_{j_y}, , s_{j_z}, s_e, s_n, s_n, s_c, s_c, s_c, s_q, s_q, s_q,\\ &s_\pi, s_\pi, s_\pi, s_\phi, s_\epsilon, s_\psi, s_\psi, s_\psi, s_\psi, s_\psi, s_\xi, s_\xi, s_\xi, s_{e^3})\end{aligned} \tag{3.4}$$

The next component concerns the values of moments at the equilibrium state and the last component that we need to specify in order to complete the MRT LBM model is the mesoscopic formulation of the forcing term. In the next section, we perform the Chapman-Enskog multiscale analysis for the $D3Q27$ model and derive the equilibrium moments and the mesoscopic formulation of the forcing term by correlating the macroscopic dynamical equations with the ones obtained from the multiscale

analysis.

$$
\mathbf{M} \equiv
\begin{array}{c|c}
 & \equiv \\
\hline
|\delta\rho\rangle & \left[\begin{array}{cccccccccccccccccccccccccc}
1 & 1 & 1 & 1 & 1 & 1 & 1 & 1 & 1 & 1 & 1 & 1 & 1 & 1 & 1 & 1 & 1 & 1 & 1 & 1 & 1 & 1 & 1 & 1 \\
\hline
0 & 1 & -1 & 0 & 0 & 0 & 1 & 1 & -1 & -1 & 1 & 1 & -1 & -1 & 0 & 0 & 0 & 1 & 1 & 1 & 1 & -1 & -1 & -1 \\
0 & 0 & 0 & 1 & -1 & 0 & 0 & 1 & 1 & -1 & 0 & 0 & 0 & 0 & 1 & 1 & -1 & -1 & 1 & 1 & -1 & -1 & -1 & -1 \\
0 & 0 & 0 & 0 & 0 & 1 & -1 & 0 & 0 & 0 & 1 & -1 & 1 & -1 & 1 & 1 & -1 & -1 & 1 & 1 & -1 & 1 & 1 & -1 \\
0 & 1 & 1 & 1 & 1 & 1 & 1 & 2 & 2 & 2 & 2 & 2 & 2 & 2 & -2 & -2 & -2 & 2 & 3 & 3 & 3 & 3 & 3 & 3 \\
0 & 2 & 2 & -1 & -1 & -1 & -1 & 1 & 1 & 1 & 1 & 1 & 1 & 1 & 0 & 0 & 0 & 0 & 0 & 0 & 0 & 0 & 0 & 0 \\
0 & 0 & 0 & 1 & 1 & -1 & -1 & 1 & 1 & 1 & -1 & -1 & -1 & -1 & 0 & 0 & 0 & 0 & 0 & 0 & 0 & 0 & 0 & 0 \\
0 & 0 & 0 & 0 & 0 & 0 & 0 & 1 & -1 & -1 & 0 & 0 & 0 & 0 & 0 & 0 & 0 & 1 & 1 & -1 & -1 & 1 & 1 & 1 \\
0 & 0 & 0 & 0 & 0 & 0 & 0 & 0 & 0 & 0 & 0 & 0 & 0 & 0 & 1 & -1 & -1 & 1 & 1 & -1 & 1 & -1 & -1 & 1 \\
0 & 0 & 0 & 0 & 0 & 0 & 0 & 0 & 0 & 0 & 1 & -1 & -1 & 1 & 0 & 0 & 0 & 1 & -1 & 1 & -1 & 1 & -1 & 1 \\
0 & 1 & -1 & 0 & 0 & 0 & 0 & 2 & -2 & -2 & 2 & 2 & -2 & -2 & 0 & 0 & 0 & 3 & 3 & 3 & -3 & -3 & -3 & -3 \\
0 & 0 & 0 & 1 & -1 & 0 & 0 & -2 & 2 & -2 & 0 & 0 & 0 & 0 & 2 & 2 & -2 & 3 & 3 & -3 & 3 & -3 & -3 & -3 \\
0 & 0 & 0 & 0 & 0 & 1 & -1 & 0 & 0 & 0 & 2 & -2 & 2 & -2 & 2 & -2 & 2 & 3 & -3 & 3 & -3 & 3 & -3 & -3 \\
0 & 0 & 0 & 0 & 0 & 0 & 0 & 1 & 1 & -1 & -1 & 1 & -1 & 1 & 0 & 0 & 0 & 0 & 0 & 0 & 0 & 0 & 0 & 0 \\
0 & 0 & 0 & 0 & 0 & 0 & 0 & 0 & 0 & 0 & 1 & 1 & 0 & 0 & 1 & -1 & -1 & 0 & 0 & 0 & 0 & 0 & 0 & 0 \\
0 & 0 & 0 & 0 & 0 & 0 & 0 & 0 & 0 & 0 & 0 & 0 & 0 & 0 & 0 & 0 & 0 & 1 & -1 & -1 & 1 & 1 & 1 & -1 \\
0 & 1 & 1 & 1 & 1 & 1 & 1 & 4 & 4 & 4 & 4 & 4 & 4 & 4 & 4 & 4 & 4 & 9 & 9 & 9 & 9 & 9 & 9 & 9 \\
0 & 2 & 2 & -1 & -1 & -1 & -1 & 2 & 2 & 2 & 2 & 2 & 2 & 2 & -4 & -4 & -4 & 0 & 0 & 0 & 0 & 0 & 0 & 0 \\
0 & 0 & 0 & 1 & 1 & -1 & -1 & 2 & 2 & 2 & -2 & -2 & -2 & -2 & 0 & 0 & 0 & 0 & 0 & 0 & 0 & 0 & 0 & 0 \\
0 & 0 & 0 & 0 & 0 & 0 & 0 & 2 & -2 & -2 & 2 & 2 & 0 & 0 & 0 & 0 & 0 & 3 & 3 & -3 & -3 & -3 & 3 & 3 \\
0 & 0 & 0 & 0 & 0 & 0 & 0 & 0 & 0 & 0 & 0 & 0 & 0 & 0 & 2 & -2 & -2 & 3 & -3 & 3 & 3 & -3 & 3 & 3 \\
0 & 0 & 0 & 0 & 0 & 0 & 0 & 0 & 0 & 0 & 2 & -2 & 2 & -2 & 0 & 0 & 0 & 3 & -3 & 3 & -3 & 3 & -3 & 3 \\
0 & 1 & -1 & 0 & 0 & 0 & 0 & 4 & 4 & -4 & 4 & 4 & -4 & -4 & 0 & 0 & 0 & 9 & 9 & 9 & -9 & -9 & -9 & -9 \\
0 & 0 & 0 & 1 & -1 & 0 & 0 & 4 & 4 & -4 & 0 & 0 & 0 & 0 & 4 & 4 & -4 & 9 & 9 & -9 & 9 & 9 & -9 & -9 \\
0 & 0 & 0 & 0 & 0 & 1 & -1 & 0 & 0 & 0 & 4 & -4 & 4 & -4 & 4 & -4 & 4 & 9 & -9 & 9 & -9 & 9 & -9 & -9 \\
0 & 1 & 1 & 1 & 1 & 1 & 1 & 8 & 8 & 8 & 8 & 8 & 8 & 8 & 8 & 8 & 8 & 27 & 27 & 27 & 27 & 27 & 27 & 27
\end{array}\right] \\
\hline
|j_x\rangle & \\
|j_y\rangle & \\
|j_z\rangle & \\
|e\rangle & \\
|p_{xx}\rangle & \\
|p_{zz}\rangle & \\
|p_{xy}\rangle & \\
|p_{yz}\rangle & \\
|p_{xz}\rangle & \\
|q_x\rangle & \\
|q_y\rangle & \\
|q_z\rangle & \\
|\pi_x\rangle & \\
|\pi_y\rangle & \\
|\pi_z\rangle & \\
|\phi_{xyz}\rangle & \\
|\epsilon\rangle & \\
|\psi_{xx}\rangle & \\
|\psi_{zz}\rangle & \\
|\psi_{xy}\rangle & \\
|\psi_{yz}\rangle & \\
|\psi_{xz}\rangle & \\
|\xi_x\rangle & \\
|\xi_y\rangle & \\
|\xi_z\rangle & \\
|e^3\rangle &
\end{array}
\tag{3.5}
$$

We further orthogonalize the rows in the matrix using the Gram-Schmidt orthogonalization and arrive at the final form of the moment matrix:

$$
\mathbf{M} \equiv \left[\begin{array}{ccccccccccccccccccccccccccc}
1 & 1 & 1 & 1 & 1 & 1 & 1 & 1 & 1 & 1 & 1 & 1 & 1 & 1 & 1 & 1 & 1 & 1 & 1 & 1 & 1 & 1 & 1 & 1 & 1 & 1 & 1 \\
0 & 1 & -1 & 0 & 0 & 0 & 0 & 1 & 1 & -1 & -1 & 1 & 1 & -1 & -1 & 0 & 0 & 0 & 0 & 1 & 1 & 1 & 1 & -1 & -1 & -1 & -1 \\
0 & 0 & 0 & 1 & -1 & 0 & 0 & 1 & -1 & 1 & -1 & 0 & 0 & 0 & 0 & 1 & 1 & -1 & -1 & 1 & 1 & -1 & -1 & 1 & 1 & -1 & -1 \\
0 & 0 & 0 & 0 & 0 & 1 & -1 & 0 & 0 & 0 & 0 & 1 & -1 & 1 & -1 & 1 & -1 & 1 & -1 & 1 & -1 & 1 & -1 & 1 & -1 & 1 & -1 \\
-2 & -1 & -1 & -1 & -1 & -1 & -1 & 0 & 0 & 0 & 0 & 0 & 0 & 0 & 0 & 0 & 0 & 0 & 0 & 1 & 1 & 1 & 1 & 1 & 1 & 1 & 1 \\
0 & 2 & 2 & -1 & -1 & -1 & -1 & 1 & 1 & 1 & 1 & 1 & 1 & 1 & 1 & -2 & -2 & -2 & -2 & 0 & 0 & 0 & 0 & 0 & 0 & 0 & 0 \\
0 & 0 & 0 & 1 & 1 & -1 & -1 & 1 & 1 & 1 & 1 & -1 & -1 & -1 & -1 & 0 & 0 & 0 & 0 & 0 & 0 & 0 & 0 & 0 & 0 & 0 & 0 \\
0 & 0 & 0 & 0 & 0 & 0 & 0 & 1 & -1 & -1 & 1 & 0 & 0 & 0 & 0 & 0 & 0 & 0 & 0 & 1 & 1 & -1 & -1 & -1 & -1 & 1 & 1 \\
0 & 0 & 0 & 0 & 0 & 0 & 0 & 0 & 0 & 0 & 0 & 0 & 0 & 0 & 0 & 1 & -1 & -1 & 1 & 1 & -1 & -1 & 1 & 1 & -1 & -1 & 1 \\
0 & 0 & 0 & 0 & 0 & 0 & 0 & 0 & 0 & 0 & 0 & 1 & -1 & -1 & 1 & 0 & 0 & 0 & 0 & 1 & -1 & 1 & -1 & -1 & 1 & -1 & 1 \\
0 & -4 & 4 & 0 & 0 & 0 & 0 & -1 & -1 & 1 & 1 & -1 & -1 & 1 & 1 & 0 & 0 & 0 & 0 & 2 & 2 & 2 & 2 & -2 & -2 & -2 & -2 \\
0 & 0 & 0 & -4 & 4 & 0 & 0 & -1 & 1 & -1 & 1 & 0 & 0 & 0 & 0 & -1 & -1 & 1 & 1 & 2 & 2 & -2 & -2 & 2 & 2 & -2 & -2 \\
0 & 0 & 0 & 0 & 0 & -4 & 4 & 0 & 0 & 0 & 0 & -1 & 1 & -1 & 1 & -1 & 1 & -1 & 1 & 2 & -2 & 2 & -2 & 2 & -2 & 2 & -2 \\
0 & 0 & 0 & 0 & 0 & 0 & 0 & 1 & 1 & -1 & -1 & -1 & -1 & 1 & 1 & 0 & 0 & 0 & 0 & 0 & 0 & 0 & 0 & 0 & 0 & 0 & 0 \\
0 & 0 & 0 & 0 & 0 & 0 & 0 & -1 & 1 & -1 & 1 & 0 & 0 & 0 & 0 & 1 & 1 & -1 & -1 & 0 & 0 & 0 & 0 & 0 & 0 & 0 & 0 \\
0 & 0 & 0 & 0 & 0 & 0 & 0 & 0 & 0 & 0 & 0 & 1 & -1 & 1 & -1 & -1 & 1 & -1 & 1 & 0 & 0 & 0 & 0 & 0 & 0 & 0 & 0 \\
0 & 0 & 0 & 0 & 0 & 0 & 0 & 0 & 0 & 0 & 0 & 0 & 0 & 0 & 0 & 0 & 0 & 0 & 0 & 1 & -1 & -1 & 1 & -1 & 1 & 1 & -1 \\
8 & 0 & 0 & 0 & 0 & 0 & 0 & -2 & -2 & -2 & -2 & -2 & -2 & -2 & -2 & -2 & -2 & -2 & -2 & 2 & 2 & 2 & 2 & 2 & 2 & 2 & 2 \\
0 & -4 & -4 & 2 & 2 & 2 & 2 & 1 & 1 & 1 & 1 & 1 & 1 & 1 & 1 & -2 & -2 & -2 & -2 & 0 & 0 & 0 & 0 & 0 & 0 & 0 & 0 \\
0 & 0 & 0 & -2 & -2 & 2 & 2 & 1 & 1 & 1 & 1 & -1 & -1 & -1 & -1 & 0 & 0 & 0 & 0 & 0 & 0 & 0 & 0 & 0 & 0 & 0 & 0 \\
0 & 0 & 0 & 0 & 0 & 0 & 0 & -2 & 2 & 2 & -2 & 0 & 0 & 0 & 0 & 0 & 0 & 0 & 0 & 1 & 1 & -1 & -1 & -1 & -1 & 1 & 1 \\
0 & 0 & 0 & 0 & 0 & 0 & 0 & 0 & 0 & 0 & 0 & 0 & 0 & 0 & 0 & -2 & 2 & 2 & -2 & 1 & -1 & -1 & 1 & 1 & -1 & -1 & 1 \\
0 & 4 & -4 & 0 & 0 & 0 & 0 & -2 & -2 & 2 & 2 & -2 & -2 & 2 & 2 & 0 & 0 & 0 & 0 & 1 & 1 & 1 & 1 & -1 & -1 & -1 & -1 \\
0 & 0 & 0 & 4 & -4 & 0 & 0 & -2 & 2 & -2 & 2 & 0 & 0 & 0 & 0 & -2 & -2 & 2 & 2 & 1 & 1 & -1 & -1 & 1 & 1 & -1 & -1 \\
0 & 0 & 0 & 0 & 0 & 4 & -4 & 0 & 0 & 0 & 0 & -2 & 2 & -2 & 2 & -2 & 2 & -2 & 2 & 1 & -1 & 1 & -1 & 1 & -1 & 1 & -1 \\
-8 & 4 & 4 & 4 & 4 & 4 & 4 & -2 & -2 & -2 & -2 & -2 & -2 & -2 & -2 & -2 & -2 & -2 & -2 & 1 & 1 & 1 & 1 & 1 & 1 & 1 & 1
\end{array}\right] \quad (3.6)
$$

3.2 Inverse Design Analysis

The Chapman-Enskog equations, which are derived in Appendix A, are as stated below:

$$O(1) : \mathbf{m}^{(0)} = \mathbf{m}^{(eq)}, \tag{3.7a}$$

$$O(\epsilon) : \left(\mathbf{I}\partial_{t1} + \hat{\mathbf{C}}_\alpha \partial_{1\alpha}\right)\mathbf{m}^{(0)} = -\frac{\mathbf{S}}{\delta_t}(\mathbf{m}^{(1)}) + \mathbf{\Psi}^{(1)}, \tag{3.7b}$$

$$O(\epsilon^2) : \partial_{t2}\mathbf{m}^{(0)} + \left(\mathbf{I}\partial_{t1} + \hat{\mathbf{C}}_\alpha \partial_{1\alpha}\right)\left[\left(1 - \frac{\mathbf{S}}{2}\right)\mathbf{m}^{(1)} + \frac{\delta_t}{2}\mathbf{\Psi}^{(1)}\right] = -\frac{\mathbf{S}}{\delta_t}\mathbf{m}^{(2)} \tag{3.7c}$$

where $\mathbf{m}^{(eq)}$ are the values of moments at equilibrium, $\mathbf{I}$ is an identity matrix, $\hat{\mathbf{C}}_\alpha \equiv \mathbf{M}$ diag$(e_{i\alpha})$ $\mathbf{M}^{-1}$, ∂_{t1} and ∂_{t2} stand for the time derivatives according to the different time scales, $\partial_{1\alpha}$ is the spatial derivative, $\mathbf{S}$ is the collision matrix and $\mathbf{\Psi}$ is the forcing term. Each equation in Eq. (3.7) is a vector equation containing 27 scalar equations. Based on the ordering of moments defined in Eq. (3.5), the first row of Eqs. (3.7b) and (3.7c) should correspond to the continuity equation. The $2^{nd}, 3^{rd}$ and 4^{th} row of Eq. (3.7b) and (3.7c) should correspond to the hydrodynamic momentum equations in x, y and z directions, respectively. Since density is a conserved moment $\rho^{(eq)} = \delta\rho$ and its relaxation parameter is irrelevant. We simply set $s_\rho = 0$. The first row of Eq. (3.7b) thus becomes

$$p\partial_{t1}\delta\rho + \partial_{1x}j_x^{(eq)} + \partial_{1y}j_y^{(eq)} + \partial_{1z}j_z^{(eq)} = \Psi_0^{(1)} \tag{3.8}$$

Eq. (3.8) should reproduce the continuity equation as stated below

$$\partial_{t1}\delta\rho + \partial_{1x}(\rho_0 u) + \partial_{1y}(\rho_0 v) + \partial_{1z}(\rho_0 w) = 0 \tag{3.9}$$

Comparing Eq. (3.8) with Eq. (3.9), we have $j_x^{(eq)} = \rho_0 u, j_y^{(eq)} = \rho_0 v$ and $j_z^{(eq)} = \rho_0 w$. The second, third and fourth row of Eq. (3.7b) become

$$\partial_{t1}(\rho_0 u_x) + \partial_{1x}\left(\frac{2}{3}\delta\rho + \frac{1}{3}e^{(eq)} + \frac{1}{3}p_{xx}^{(eq)}\right) + \partial_{1y}\left(p_{xy}^{(eq)}\right) + \partial_{1z}\left(p_{xz}^{(eq)}\right) = -\frac{s_{j_x}}{\delta_t}j_x^{(1)} + \Psi_1^{(1)} \tag{3.10a}$$

$$\partial_{t1}(\rho_0 u_y) + \partial_{1x}\left(p_{xy}^{(eq)}\right) + \partial_{1y}\left(\frac{2}{3}\delta\rho - \frac{1}{6}p_{xx}^{(eq)} + \frac{1}{2}p_{zz}^{(eq)} + \frac{1}{3}e^{(eq)}\right) + \partial_{1z}\left(p_{yz}^{(eq)}\right) = -\frac{s_{j_y}}{\delta_t}j_y^{(1)} + \Psi_2^{(1)} \tag{3.10b}$$

$$\partial_{t1}(\rho_0 u_z)+\partial_{1x}\left(p_{xz}^{(eq)}\right)+\partial_{1y}\left(p_{yz}^{(eq)}\right)+\partial_{1z}\left(\frac{2}{3}\delta\rho-\frac{1}{6}p_{xx}^{(eq)}-\frac{1}{2}p_{zz}^{(eq)}+\frac{1}{3}e^{(eq)}\right)=-\frac{s_{j_z}}{\delta_t}j_z^{(1)}+\Psi_3^{(1)} \tag{3.10c}$$

The above equations must match the Euler momentum equations

$$\partial_{t1}(\rho_0 u_x)+\partial_{1x}\left(p+\rho_0 u_x^2\right)+\partial_{1y}\left(\rho_0 u_x u_y\right)+\partial_{1z}\left(\rho_0 u_x u_z\right)=F_x^{(1)} \tag{3.11a}$$

$$\partial_{t1}(\rho_0 u_y)+\partial_{1x}\left(\rho_0 u_x u_y\right)+\partial_{1y}\left(p+\rho_0 u_y^2\right)+\partial_{1z}\left(\rho_0 u_y u_z\right)=F_y^{(1)} \tag{3.11b}$$

$$\partial_{t1}(\rho_0 u_z)+\partial_{1x}\left(\rho_0 u_x u_z\right)+\partial_{1y}\left(\rho_0 u_y u_z\right)+\partial_{1z}\left(p+\rho_0 u_z^2\right)=F_z^{(1)} \tag{3.11c}$$

In Eq. (3.11) the pressure is calculated from the ideal gas equation of state i.e. $p=\delta\rho c_s^2$, where c_s is the speed of sound. By comparing the LHS of Eqs. (3.10) and (3.11), we can write down six equations. These can be used to obtain the following six moments as

$$p_{xx}^{(eq)}=\rho_0\left(2u_x^2-u_y^2-u_z^2\right) \tag{3.12a}$$

$$e^{(eq)}=\left(3c_s^2-2\right)\delta\rho+\rho_0\left(u_x^2+u_y^2+u_z^2\right) \tag{3.12b}$$

$$p_{zz}^{(eq)}=\rho_0\left(u_y^2-u_z^2\right) \tag{3.12c}$$

$$p_{xy}^{(eq)}=\rho_0 uv,\ p_{yz}^{(eq)}=\rho_0 vw,\ p_{xz}^{(eq)}=\rho_0 uw \tag{3.12d}$$

By comparing the RHS of Eqs. (3.10) with (3.11), we have:

$$-\frac{s_{j_x}}{\delta_t}j_x^{(1)}+\Psi_1^{(1)}=F_x^{(1)} \tag{3.13a}$$

$$-\frac{s_{j_y}}{\delta_t}j_y^{(1)}+\Psi_2^{(1)}=F_y^{(1)} \tag{3.13b}$$

$$-\frac{s_{j_z}}{\delta_t} j_z^{(1)} + \Psi_3^{(1)} = F_z^{(1)} \tag{3.13c}$$

By manipulating the equations obtained from rows 5 - 10 of (3.7b), related to the evolution of second-order moments and plugging in Euler's equation, we have:

$$\begin{aligned} \partial_{1x}\left(\frac{1}{3}\rho_0 u_x + \frac{1}{3}q_x^{(eq)}\right) + \partial_{1y}\left(\frac{1}{3}\rho_0 u_y + \frac{1}{3}q_y^{(eq)}\right) + \partial_{1z}\left(\frac{1}{3}\rho_0 u_z + \frac{1}{3}q_z^{(eq)}\right) \\ = -\frac{s_e}{\delta_t}\big(e^{(1)}\big) + \Psi_4^{(1)} - 2(u_x F_x + u_y F_y + u_z F_z) \end{aligned} \tag{3.14a}$$

$$\begin{aligned} \partial_{1x}\left(\frac{2}{3}\rho_0 u_x - \frac{1}{3}q_x^{(eq)}\right) + \partial_{1y}\left(-\frac{1}{3}\rho_0 u_y + \frac{1}{6}q_y^{(eq)} - \frac{3}{2}\pi_y^{(eq)}\right) + \partial_{1z}\left(-\frac{1}{3}\rho_0 u_z + \frac{1}{6}q_z^{(eq)} + \frac{3}{2}\pi_z^{(eq)}\right) \\ = -\frac{s_n}{\delta_t}\big(p_{xx}^{(1)}\big) + \Psi_5^{(1)} - 2(2u_x F_x - u_y F_y - u_z F_z) \end{aligned} \tag{3.14b}$$

$$\begin{aligned} \partial_{1x}\big(\pi_x^{(eq)}\big) + \partial_{1y}\left(\frac{1}{3}\rho_0 u_y - \frac{1}{6}q_y^{(eq)} - \frac{1}{2}\pi_y^{(eq)}\right) + \partial_{1z}\left(-\frac{1}{3}\rho_0 u_z + \frac{1}{6}q_z^{(eq)} - \frac{1}{2}\pi_z^{(eq)}\right) \\ = -\frac{s_n}{\delta_t}\big(p_{zz}^{(1)}\big) + \Psi_6^{(1)} - 2(u_y F_y - u_z F_z) \end{aligned} \tag{3.14c}$$

$$\begin{aligned} \partial_{1x}\left(\frac{2}{3}\rho_0 u_y + \frac{1}{6}q_y^{(eq)} - \frac{1}{2}\pi_y^{(eq)}\right) + \partial_{1y}\left(\frac{2}{3}\rho_0 u_x + \frac{1}{6}q_x^{(eq)} + \frac{1}{2}\pi_x^{(eq)}\right) + \partial_{1z}\big(\phi_{xyz}^{(eq)}\big) \\ = -\frac{s_c}{\delta_t}\big(p_{xy}^{(1)}\big) + \Psi_7^{(1)} - (u_x F_x + u_y F_y) \end{aligned} \tag{3.14d}$$

$$\begin{aligned} \partial_{1x}\big(\phi_{xyz}^{(eq)}\big) + \partial_{1y}\left(\frac{2}{3}\rho_0 u_z + \frac{1}{6}q_y^{(eq)} - \frac{1}{2}\pi_z^{(eq)}\right) + \partial_{1z}\left(\frac{2}{3}\rho_0 u_y + \frac{1}{6}q_y^{(eq)} + \frac{1}{2}\pi_y^{(eq)}\right) \\ = -\frac{s_c}{\delta_t}\big(p_{yz}^{(1)}\big) + \Psi_8^{(1)} - (u_y F_y + u_z F_z) \end{aligned} \tag{3.14e}$$

$$\begin{aligned} \partial_{1x}\left(\frac{2}{3}\rho_0 u_z + \frac{1}{6}q_z^{(eq)} + \frac{1}{2}\pi_z^{(eq)}\right) + \partial_{1y}\big(\phi_{xyz}^{(eq)}\big) + \partial_{1z}\left(\frac{2}{3}\rho_0 u_x + \frac{1}{6}q_x^{(eq)} - \frac{1}{2}\pi_x^{(eq)}\right) \\ = -\frac{s_c}{\delta_t}\big(p_{xz}^{(1)}\big) + \Psi_9^{(1)} - (u_x F_x + u_z F_z) \end{aligned} \tag{3.14f}$$

Next, let us look at the moment equations of order $O(\epsilon^2)$

$$O(\epsilon^2) : \partial_{t2}\mathbf{m}^{(0)} + \big(\mathbf{I}\partial_{t1} + \hat{\mathbf{C}}_\alpha \partial_{1\alpha}\big)\left[\left(1 - \frac{\mathbf{S}}{2}\right)\mathbf{m}^{(1)} + \frac{\delta_t}{2}\mathbf{\Psi}^{(1)}\right] = -\frac{\mathbf{S}}{\delta_t}\mathbf{m}^{(2)} \tag{3.15}$$

For simplicity, let us denote

$$\mathbf{A} \equiv \left(I - \frac{\mathbf{S}}{2}\right)\mathbf{m}^{(1)} + \frac{\delta_t}{2}\mathbf{\Psi}^{(1)} \tag{3.16}$$

This simplifies Eq. (3.15) to

$$O(\epsilon^2) : \partial_{t2}\mathbf{m}^{(0)} + \big(\mathbf{I}\partial_{t1} + \hat{\mathbf{C}}_\alpha \partial_{1\alpha}\big)\mathbf{A} = -\frac{\mathbf{S}}{\delta_t}\mathbf{m}^{(2)} \tag{3.17}$$

The first row of Eq. (3.17) gives:

$$\partial_{t2}(\rho_0 u_x) + \partial_{1x}A_{j_x} + \partial_{1y}A_{j_y} + \partial_{1z}A_{j_z} = 0 \tag{3.18}$$

The above equation should match with the continuity equation at $O(\epsilon^2)$, i.e. $\partial_{t2}\delta\rho = 0$. Therefore, $A_{j_x} = A_{j_y} = A_{j_z} = 0$, and the following three constraints are thus obtained

$$\left(1 - \frac{s_{j_x}}{2}\right)j_x^{(1)} + \frac{\delta_t}{2}\Psi_1^{(1)} = 0 \tag{3.19a}$$

$$\left(1 - \frac{s_{j_y}}{2}\right)j_y^{(1)} + \frac{\delta_t}{2}\Psi_2^{(1)} = 0 \tag{3.19b}$$

$$\left(1 - \frac{s_{j_z}}{2}\right)j_z^{(1)} + \frac{\delta_t}{2}\Psi_3^{(1)} = 0 \tag{3.19c}$$

Solving, the two sets of Eqs. (3.13) and (3.19), we have

$$\Psi_1^{(1)} = F_x^{(1)}\left(1 - \frac{s_{j_x}}{2}\right), \Psi_2^{(1)} = F_y^{(1)}\left(1 - \frac{s_{j_y}}{2}\right), \Psi_3^{(1)} = F_z^{(1)}\left(1 - \frac{s_{j_z}}{2}\right) \tag{3.20a}$$

$$j_x^{(1)} = -\frac{F_x^{(1)}\delta_t}{2},\ j_y^{(1)} = -\frac{F_y^{(1)}\delta_t}{2},\ j_z^{(1)} = -\frac{F_z^{(1)}\delta_t}{2} \tag{3.20b}$$

The $2^{nd}, 3^{rd}$ and 4^{th} row of Eq. (3.17) are

$$\partial_{t2}\big(\rho_0 u_x\big) + \partial_{t1}A_{j_x} + \partial_{1x}\left(\frac{1}{3}A_{p_{xx}} + \frac{1}{3}A_e\right) + \partial_{1y}\big(A_{p_{xy}}\big) + \partial_{1z}\big(A_{p_{xz}}\big) = 0 \tag{3.21a}$$

$$\partial_{t2}\big(\rho_0 u_y\big)+\partial_{t1}A_{j_y}+\partial_{1x}\big(A_{p_{xy}}\big)+\partial_{1y}\bigg(-\frac{1}{6}A_{p_{xx}}+\frac{1}{2}A_{p_{zz}}+\frac{1}{3}A_e\bigg)+\partial_{1z}\big(A_{p_{yz}}\big)=0 \quad (3.21b)$$

$$\partial_{t2}\big(\rho_0 u_z\big)+\partial_{t1}A_{j_z}+\partial_{1x}\big(A_{p_{xz}}\big)+\partial_{1y}\big(A_{p_{yz}}\big)+\partial_{1z}\bigg(-\frac{1}{6}A_{p_{xx}}-\frac{1}{2}A_{p_{zz}}+\frac{1}{3}A_e\bigg)=0 \quad (3.21c)$$

By comparing Eqs. (3.21) with the Navier-Stokes equations of order $O(\epsilon^2)$

$$\begin{aligned}\partial_{t2}(\rho_0 u_x)-\partial_{1x}\bigg[\mu^V\bigtriangledown_1\mathbf{u}+\mu\bigg(\frac{4}{3}\partial_{1x}u_x-\frac{2}{3}\partial_{1y}u_y-\frac{2}{3}\partial_{1z}u_z\bigg)\bigg]\\ -\mu\partial_{1y}(\partial_{1y}u_x+\partial_{1x}u_y)-\mu\partial_{1z}(\partial_{1z}u_x+\partial_{1x}u_z)=0\end{aligned} \quad (3.22a)$$

$$\begin{aligned}\partial_{t2}(\rho_0 u_y)-\partial_{1y}\bigg[\mu^V\bigtriangledown_1\mathbf{u}+\mu\bigg(\frac{4}{3}\partial_{1x}u_y-\frac{2}{3}\partial_{1y}u_x-\frac{2}{3}\partial_{1z}u_z\bigg)\bigg]\\ -\mu\partial_{1x}(\partial_{1y}u_x+\partial_{1x}u_y)-\mu\partial_{1z}(\partial_{1z}u_y+\partial_{1y}u_z)=0\end{aligned} \quad (3.22b)$$

$$\begin{aligned}\partial_{t2}(\rho_0 u_z)-\partial_{1z}\bigg[\mu^V\bigtriangledown_1\mathbf{u}+\mu\bigg(\frac{4}{3}\partial_{1x}u_z-\frac{2}{3}\partial_{1y}u_y-\frac{2}{3}\partial_{1z}u_x\bigg)\bigg]\\ -\mu\partial_{1x}(\partial_{1y}u_z+\partial_{1z}u_y)-\mu\partial_{1y}(\partial_{1z}u_x+\partial_{1x}u_z)=0\end{aligned} \quad (3.22c)$$

where $\bigtriangledown_1 u\equiv\partial_{1x}u_x+\partial_{1y}u_y+\partial_{1z}u_z$, μ and μ^V are the dynamic shear and bulk viscosity, respectively. It follows that

$$j_x^{(2)}=j_y^{(2)}=j_z^{(2)}=0 \quad (3.23a)$$

$$A_e=-3\mu^V\big(\frac{\partial u_x}{\partial x}+\frac{\partial u_y}{\partial y}+\frac{\partial u_z}{\partial z}\big) \quad (3.23b)$$

$$A_{p_{xx}}=-2\mu\big(2\frac{\partial u_x}{\partial x}-\frac{\partial u_y}{\partial y}-\frac{\partial u_z}{\partial z}\big) \quad (3.23c)$$

$$A_{p_{xx}}=-2\mu\big(\frac{\partial u_y}{\partial y}-\frac{\partial u_z}{\partial z}\big) \quad (3.23d)$$

$$A_{p_{xy}}=-\mu\bigg(\frac{\partial u_x}{\partial y}+\frac{\partial u_y}{\partial x}\bigg),\ A_{p_{xz}}=-\mu\bigg(\frac{\partial u_x}{\partial z}+\frac{\partial u_z}{\partial x}\bigg),\ A_{p_{yz}}=-\mu\bigg(\frac{\partial u_y}{\partial z}+\frac{\partial u_z}{\partial y}\bigg) \quad (3.23e)$$

In Eq. (3.16), we have expressed $\mathbf{A}$ as functions of forcing components $\mathbf{\Psi}$ and non-equilibrium moments $\mathbf{m}^{(1)}$. Re-arranging Eq. (3.7b), $\mathbf{m}^{(1)}$ can be obtained in terms of equilibrium moment and the forcing term

$$\mathbf{m}^{(1)} = \delta_t \mathbf{S}^{-1}\left[\mathbf{\Psi}^{(1)} - (I\partial_{t1} + \hat{\mathbf{C}}_\alpha \partial_{1\alpha})\mathbf{m}^{(eq)}\right] \tag{3.24}$$

Now, substituting Eq. (3.24) into Eq. (3.16), we can express $\mathbf{A}$ as

$$\mathbf{A} = \delta_t \mathbf{S}^{-1}\mathbf{\Psi}^{(\mathbf{1})} - \left(\mathbf{S}^{-1} - \frac{1}{2}\right)(\mathbf{I}\partial_{t1} + \hat{\mathbf{C}}_\alpha \partial_{1\alpha})\mathbf{m}^{(eq)} \tag{3.25}$$

A comparison of Eqs. (3.23) and (3.25) allows us to design the equilibrium moments and forcing terms such that they follow the Navier-Stokes equation. We should also note that the mesoscopic forcing term $\mathbf{\Psi}^{(1)}$ reproduces the macroscopic force. Therefore we state two basic conditions: (a) all terms that contain macroscopic force $\mathbf{F}$ and mesoscopic forcing term $\mathbf{\Psi}$ should balance each other and (b) they should be treated seperately. Now, let us expand rows 5 - 10 of Eq. (3.25)

$$A_e = -\left(\frac{2-s_e}{2s_e}\right)\delta_t\Bigg\{\partial_{1x}\left[\frac{1}{3}\rho_0 u_x + \frac{1}{3}q_x^{(eq)} - \big(3c_s^2 - 2\big)\rho_0 u_x\right] + \partial_{1y}\left[\frac{1}{3}\rho_0 u_y + \frac{1}{3}q_y^{(eq)} - \big(3c_s^2 - 2\big)\rho_0 u_y\right] + \partial_{1z}\left[\frac{1}{3}\rho_0 u_z + \frac{1}{3}q_z^{(eq)} - \big(3c_s^2 - 2\big)\rho_0 u_z\right]\Bigg\} \tag{3.26a}$$

$$A_{p_{xx}} = -\left(\frac{2-s_n}{2s_n}\right)\delta_t\Bigg\{\partial_{1x}\left[\frac{2}{3}\rho_0 u_x - \frac{1}{3}q_x^{(eq)}\right] + \partial_{1y}\left[-\frac{1}{3}\rho_0 u_y + \frac{1}{6}q_y^{(eq)} - \frac{3}{2}\pi_y^{(eq)}\right] + \partial_{1z}\left[-\frac{1}{3}\rho_0 u_z + \frac{1}{6}q_z^{(eq)} + \frac{3}{2}\pi_z^{(eq)}\right]\Bigg\} \tag{3.26b}$$

$$A_{p_{zz}} = -\left(\frac{2-s_n}{2s_n}\right)\delta_t\Bigg\{\partial_{1x}\pi_x^{(eq)} + \partial_{1y}\left[\frac{1}{3}\rho_0 u_y - \frac{1}{6}q_y^{(eq)} - \frac{1}{2}\pi_y^{(eq)}\right] + \partial_{1z}\left[-\frac{1}{3}\rho_0 u_z + \frac{1}{6}q_z^{(eq)} - \frac{1}{2}\pi_z^{(eq)}\right]\Bigg\} \tag{3.26c}$$

$$A_{p_{xy}} = -\left(\frac{2-s_c}{2s_c}\right)\delta_t\Bigg\{\partial_{1x}\left[\frac{2}{3}\rho_0 u_y + \frac{1}{3}q_y^{(eq)} - \frac{1}{2}\pi_y^{(eq)}\right] + \partial_{1y}\left[\frac{2}{3}\rho_0 u_x + \frac{1}{6}q_x^{(eq)} - \frac{1}{2}\pi_x^{(eq)}\right] + \partial_{1z}\phi_{xyz}^{(eq)}\Bigg\} \tag{3.26d}$$

$$A_{p_{yz}} = -\left(\frac{2-s_c}{2s_c}\right)\delta_t\Bigg\{\partial_{1x}\phi^{(eq)}_{xyz} + \partial_{1y}\left[\frac{2}{3}\rho_0 u_z + \frac{1}{6}q^{(eq)}_y - \frac{1}{2}\pi^{(eq)}_z\right] + \partial_{1z}\left[\frac{2}{3}\rho_0 u_y + \frac{1}{6}q^{(eq)}_y + \frac{1}{2}\pi^{(eq)}_y\right]\Bigg\} \tag{3.26e}$$

$$A_{p_{xz}} = -\left(\frac{2-s_c}{2s_c}\right)\delta_t\Bigg\{\partial_{1x}\left[\frac{2}{3}\rho_0 u_z + \frac{1}{6}q^{(eq)}_z + \frac{1}{2}\pi^{(eq)}_z\right] + \partial_{1y}\phi^{(eq)}_{xyz} + \partial_{1z}\left[\frac{2}{3}\rho_0 u_x + \frac{1}{6}q^{(eq)}_x - \frac{1}{2}\pi^{(eq)}_x\right]\Bigg\} \tag{3.26f}$$

Comparing the above equations with Eq. (3.23 b - d) we can design the equilibrium values of moments as $q^{(eq)}_x = a\rho_0 u_x$, $q^{(eq)}_y = a\rho_0 u_y$, $q^{(eq)}_z = a\rho_0 u_z$, $\pi^{(eq)}_x = 0$, $\pi^{(eq)}_y = b\rho_0 u_y$, $\pi^{(eq)}_z = c\rho_0 u_z$ where a, b and c are random constants. By comparing the coefficients of the different flux terms of both sets of equations we get the values of $a = -2$, $b = c = 0$. From the shear stress group we derive the final equilibrium value of moment which affects the macroscopic hydrodynamics equations i.e. $\phi^{(eq)}_{xyz} = 0$.

We derive the forcing terms $\mathbf{\Psi}^{(1)}$ by using the two basic conditions relating the mesoscopic and the macroscopic forcing terms:

$$\Psi^{(1)}_4 = -2\left(1 - \frac{s_e}{2}\right)(u_x F_x + u_y F_y + u_z F_z) \tag{3.27a}$$

$$\Psi^{(1)}_5 = -2\left(1 - \frac{s_n}{2}\right)(2u_x F_x - u_y F_y - u_z F_z) \tag{3.27b}$$

$$\Psi^{(1)}_6 = -2\left(1 - \frac{s_n}{2}\right)(u_y F_y - u_z F_z) \tag{3.27c}$$

$$\Psi^{(1)}_7 = -2\left(1 - \frac{s_c}{2}\right)(u_x F_x + u_y F_y) \tag{3.27d}$$

$$\Psi^{(1)}_8 = -2\left(1 - \frac{s_c}{2}\right)(u_y F_y + u_z F_z) \tag{3.27e}$$

$$\Psi^{(1)}_9 = -2\left(1 - \frac{s_c}{2}\right)(u_x F_x + u_z F_z) \tag{3.27f}$$

To summarize, we have derived the equilibrium values of moments up to the third order. These are the moments that affect the macroscopic hydrodynamic equations. The remaining moments do not affect the Navier-Stokes equations, so in principle they can be of any value. In this model we obtain all their values according to the BGK distributions, as discussed in Sec. 2.3. Similarly, the mesoscopic forcing terms which affect the hydrodynamics of the flow problem have all been derived. The remaining forcing terms can be set equal to zero since they do not affect the hydrodynamic equations in any way. The details that are needed to summarize the model are as listed below:

$$\mathbf{m}^{(eq)} = \begin{bmatrix} 0 \\ 0 \\ 0 \\ 0 \\ (3c_s^2 - 2)\delta\rho + \rho_0(u_x^2 + u_y^2 + u_z^2) \\ \rho_0(2u_x^2 - u_y^2 - u_z^2) \\ \rho_0(u_y^2 - u_z^2) \\ \rho_0 u_x u_y \\ \rho_0 u_y u_z \\ \rho_0 u_x u_z \\ -2\rho_0 u_x \\ -2\rho_0 u_y \\ -2\rho_0 u_z \\ 0 \\ 0 \\ 0 \\ 0 \\ 2\delta\rho - 4\rho_0(u_x^2 + u_y^2 + u_z^2) \\ -\rho_0(2u_x^2 - u_y^2 - u_z^2) \\ -\rho_0(u_y^2 - u_z^2) \\ -\rho_0 u_x u_y \\ -\rho_0 u_y u_z \\ -\rho_0 u_x u_z \\ \rho_0 u_x \\ \rho_0 u_y \\ \rho_0 u_z \\ -\delta\rho + 3\rho_0(u_x^2 + u_y^2 + u_z^2) \end{bmatrix} \tag{3.28a}$$

$$\boldsymbol{\Psi}^{(1)} = \begin{bmatrix} 0 \\ F_x^{(1)}\left(1-\frac{s_{jx}}{2}\right) \\ F_y^{(1)}\left(1-\frac{s_{jy}}{2}\right) \\ F_z^{(1)}\left(1-\frac{s_{jz}}{2}\right) \\ -2\left(1-\frac{s_e}{2}\right)(u_xF_x+u_yF_y+u_zF_z) \\ -2\left(1-\frac{s_n}{2}\right)(2u_xF_x-u_yF_y-u_zF_z) \\ -2\left(1-\frac{s_n}{2}\right)(u_yF_y-u_zF_z) \\ -\left(1-\frac{s_c}{2}\right)(u_xF_x+u_yF_y) \\ -\left(1-\frac{s_c}{2}\right)(u_yF_y+u_zF_z) \\ -\left(1-\frac{s_c}{2}\right)(u_xF_x+u_zF_z) \\ 0 \\ . \\ . \\ . \\ 0 \end{bmatrix} \tag{3.28b}$$

3.3 Boundary Conditions

The most popular set of boundary conditions used while trying to simulate fluid flow phenomena at the solid-fluid interface is the bounce back scheme [35]

$$f_{\tilde{\alpha}}(\mathbf{r}_f, t+\Delta t) = \tilde{f}_\alpha(\mathbf{r}_f, t) - (\tilde{f}_\alpha^{(eq)}(\mathbf{r}_w, t^+) - f_{\tilde{\alpha}}^{(eq)}(\mathbf{r}_w, t^+)) = \tilde{f}_\alpha(\mathbf{r}_f, t) + 2w_\alpha\rho_0\frac{\mathbf{e}_{\tilde{\alpha}}\cdot\mathbf{u}_w}{c_s^2} \tag{3.29}$$

where $\mathbf{r}_f$ indicates the boundary fluid node as shown in Fig. 3.1, $\mathbf{e}_\alpha$ points into the solid region and $e_{\tilde{\alpha}} = -\mathbf{e}_\alpha$, t^+ denotes the time when the distribution $\tilde{f}_\alpha(\mathbf{r}_f, t)$ arrives at the fluid-solid boundary. The simplest bounce back scheme, Eq. (3.28), is of second-order accuracy when the solid boundary is located half way between the lattice node at the boundary and its subsequent node. However, when the boundary is not exactly midway from the boundary node, the accuracy is of first order which is inconsistent

with the design of the LB equation. To capture the actual shape of the solid boundary and maintain the second-order accuracy, an interpolation scheme is used to find the missing distribution function $f_{\tilde{\alpha}}(\mathbf{r}_f, t + \Delta t)$. The interpolation scheme that is used in our study is the Yu et al.'s double interpolation scheme [36].

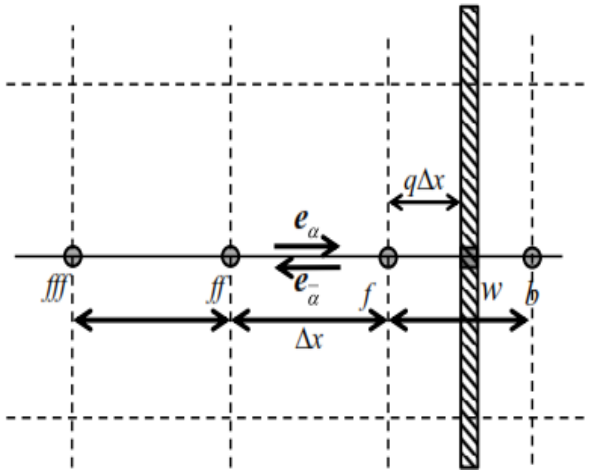

Figure 3.1: Sketch to show notations used to construct a bounce back scheme at the fluid-solid boundary.

3.3.1 Yu's Double Interpolation

For this boundary treatment, we need to go through three steps: By using the existing populations at the nodes f, ff and fff for e_α, the population at a temporary location (distance Δx from the wall boundary w) is interpolated, during the streaming process [36]. After streaming the populations would propagate exactly to the wall.

$$Linear : \tilde{f}_\alpha(\mathbf{r}_w, t + \Delta t) = q\tilde{f}_\alpha(\mathbf{r}_f, t) + (1 - q)\tilde{f}_\alpha(\mathbf{r}_{ff}, t) \tag{3.30a}$$

$$Quadratic : f_\alpha(\mathbf{r}_w, t+\Delta t) = \frac{q(1+q)}{2}\tilde{f}_\alpha(\mathbf{r}_f, t)+(1-q)(1+q)\tilde{f}_\alpha(\mathbf{r}_{ff}, t)-\frac{q(1-q)}{2}\tilde{f}_\alpha(\mathbf{r}_{fff}, t) \tag{3.30b}$$

The next step is an instantaneous bounce-back operation at the wall

$$f_{\tilde{\alpha}}(\mathbf{r}_w, t + \Delta t) = f_\alpha(\mathbf{r}_w, t + \Delta t) + 2w_\alpha\rho_0\frac{\mathbf{e}_{\tilde{\alpha}} \cdot \mathbf{u}_w}{c_s^2} \tag{3.31}$$

Eventually, the unknown population is interpolated from $f_{\tilde{\alpha}}(\mathbf{r}_w, t+\Delta t)$, $f_{\tilde{\alpha}}(\mathbf{r}_{ff}, t+\Delta t)$ and $f_{\tilde{\alpha}}(\mathbf{r}_{fff}, t+\Delta t)$

$$Linear : f_{\tilde{\alpha}}(\mathbf{r}_f, t+\Delta t) = \frac{1}{1+q} f_{\tilde{\alpha}}(\mathbf{r}_w, t+\Delta t) + \frac{q}{1+q} f_{\tilde{\alpha}}(\mathbf{r}_{ff}, t+\Delta t) \tag{3.32a}$$

$$Quadratic : f_{\tilde{\alpha}}(\mathbf{r}_f, t+\Delta t) = \frac{2}{(1+q)(2+q)} f_{\tilde{\alpha}}(\mathbf{r}_w, t+\Delta t) + \frac{2q}{1+q} f_{\tilde{\alpha}}(\mathbf{r}_{ff}, t+\Delta t) - \frac{q}{2+q} f_{\tilde{\alpha}}(\mathbf{r}_{fff}, t+\Delta t) \tag{3.32b}$$

3.4 LBM Algorithm

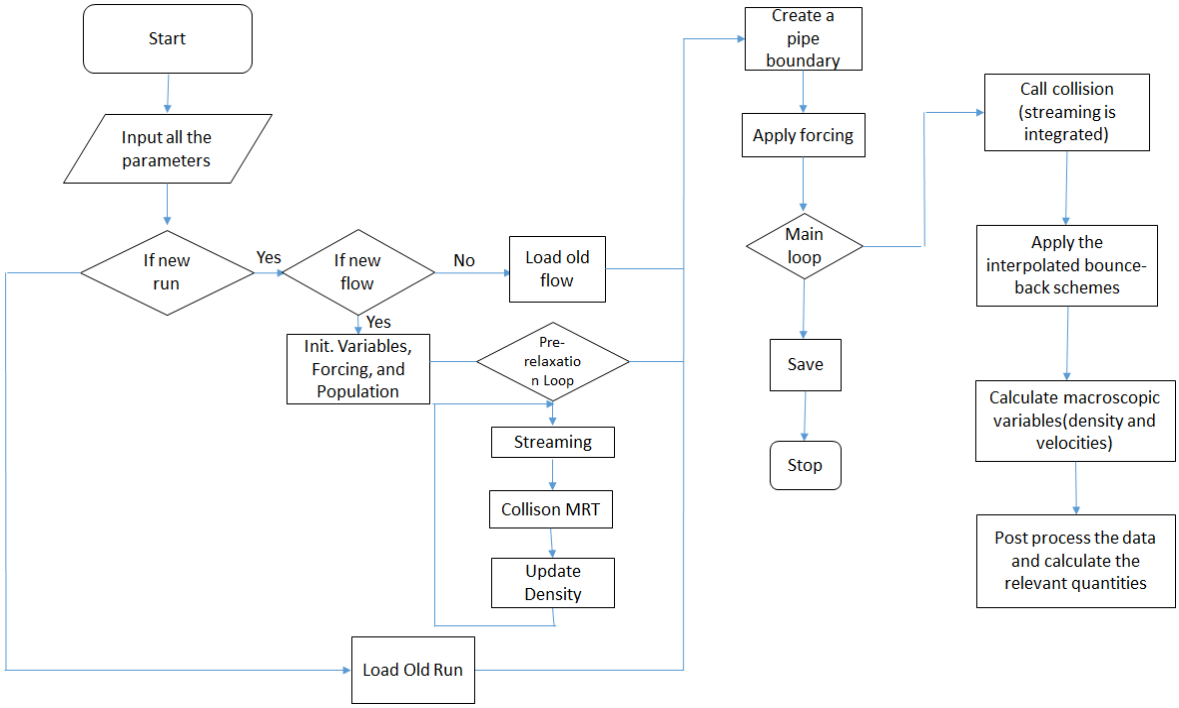

Figure 3.2: Flowchart representing the algorithm of the code, incorporating the lattice Boltzmann solver.

Fig. 3.2 is a flowchart representing the algorithm of the lattice Boltzmann solver. This algorithm is implemented in a code written in FORTRAN and MPI, whose most important feature is the one step implementation of both streaming and collision stages. This implementation helps us make the code faster and more efficient by reducing data dependency between the collision statement and the streaming statement.

Chapter 4

RESULTS

4.1 Validation of the D3Q27 Model: Unsteady Laminar Flow Results

4.1.1 Unsteady Laminar Channel Flow Results

First, we use the two-dimensional, unsteady, laminar channel flow to validate the $D3Q27$ model in the presence of flat solid walls. The Reynolds number(Re) based on the maximum center line velocity attained by the flow and the half channel width is 20. The flow begins from rest and is driven by a constant body force until it reaches the steady state. The body force could represent the pressure difference at the two ends of the channel. This body force can be written as

$$F_y = \frac{8\rho_0 \nu V_{max}}{H^2} \tag{4.1}$$

where V_{max} is the maximum velocity at the channel centerline, at steady state, ν is the kinematic viscosity and H is the channel height. Since the flow is laminar, there is no variation in the streamise or the spanwise direction. We only need to resolve the flow in the transverse direction. Hence, the grid resolutions in the streamwise and the spanwise direction are comparitively smaller than the grid resolution in the transverse direction. The computational domain size for this case is set to $N_x \times N_y \times N_z = 40 \times 8 \times 8$. The height of the channel is thus $H = 40\Delta x$, where Δx is the size of the grid-spacing. The mid-link bounce back scheme is applied to fulfill the no-slip boundary condition by placing the wall boundary half lattice away from the boundary fluid nodes. At the boundary node, the outward post-streaming distribution is equal to the inward pre-streaming distribution i.e. $f_{\tilde{i}}(\mathbf{r}_b, t + \Delta t) = f_i(\mathbf{r}_b, t)$ where $\mathbf{r}_b$ is the location of a boundary node, f_i represents the pre-streaming distribution function with particle

velocity $\mathbf{e}_i$, which points into the wall. $f_{\bar{i}}$ represents the post-streaming distribution function in the direction opposite to $\mathbf{e}_i$. We apply periodic boundary conditions in both the streamwise and spanwise directions. In the code, x, y and z represent the transverse, streamwise, and spanwise direction, respectively. The maximum streamwise velocity V_{max} is set to 0.05 and the speed of sound c_s is 0.5773. Hence, the maximum Mach number is much smaller than 1/3. The kinematic shear viscosity is calculated by using the definition of the Reynolds number

$$\nu = \frac{V_{max} H}{Re}, \tag{4.2}$$

The relaxation parameters introduced in Sec. 3.1 are then given by the relation

$$\mathbf{s} = \frac{1}{3\nu + 0.5} \tag{4.3}$$

The results obtained from the simulation are then compared with the analytical results obtained from solving the Navier-Stokes equation. For a laminar channel flow, the Navier-Stokes equation reduces to a PDE where the velocity field is a function of the time and distance from the channel wall. The PDE is solved using separation of variables and the result is given as

$$u_{theory} = \sum_{n=1}^{\infty} \frac{32}{k_n^3} \left[1 - exp\left(- \frac{k_n^2 \nu t}{H^2} \right) \right] sin\left[\frac{k_n (x - 0.5)}{H} \right] \tag{4.4}$$

where $k_n = (2n - 1)\pi$. t is the number of the time step, x represents the coordinate index of a specified point normal to the wall. Thus $(x - 0.5)$ is the position of this point in the physical space since the physical position is located at the center of lattice, which is half grid from the boundary. In the simulation, it is impossible to sum infinite terms to get the theoretical solution of velocity. Therefore, only the first 300 terms of the analytical solution are summed to get the analytical result at a certain time and position.

In Fig. 4.1, the time evolution of the streamwise velocity close to the channel centerline has been plotted. The theoretical velocity at this location is also plotted as the benchmark. We can see that the value of the streamwise velocity close to the

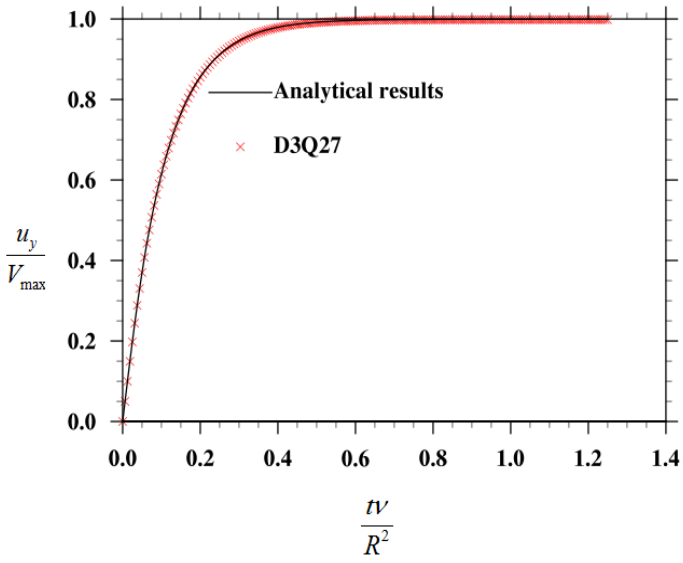

Figure 4.1: Time evolution of the streamwise velocity at $x/H = 0.4875$(close to the channel centerline). All the values are normalized as indicated.

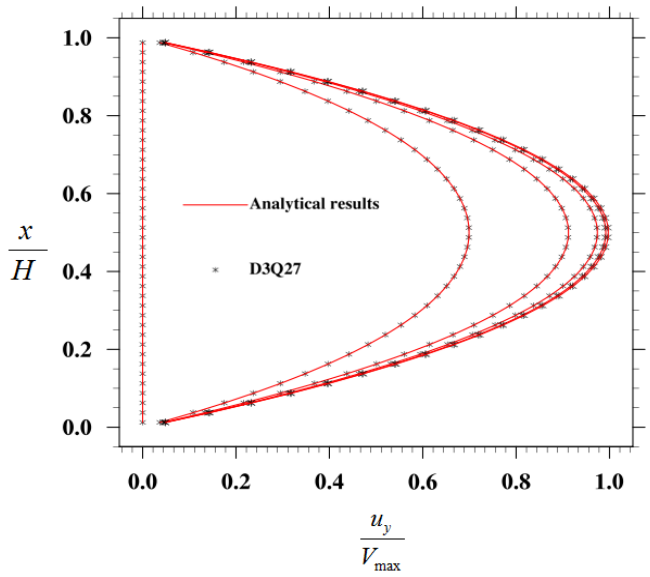

Figure 4.2: Streamwise velocity profiles at six different times, $t\nu/H^2 = 0$, 0.125, 0.25, 0.375, 0.5 and 0.625. All the values are normalized as indicated.

channel centerline steadily increases from 0 to 1 under the application of a constant uniform external force. The steady-state velocity is reached at roughly $\frac{t\nu}{H^2} = 0.5$ (see Fig. 4.1). At the location $\frac{x}{H} = 0.4875$, which is close to the channel centerline, the value of $\frac{u_y}{V_{max}}$ is very close to 1, but not exactly equal. In Fig 4.1, we see good agreement between the simulation results and the benchmark.

In Fig. 4.2, we plot the profiles of the streamwise velocity $\frac{u_y}{V_{max}}$ at different times $t\nu/H^2 = 0$, 0.125, 0.25, 0.375, 0.5 and 0.625. We also plot the analytical results at the given times as the benchmark. From Fig. 4.2, we can see excellent agreement between the analytical and the simulation results. The flow starts from rest and has already reached the steady state at $t\nu/H^2 = 0.625$. This can be deduced from the fact that the maximum value of the streamwise velocity is equal to one at the position $\frac{x}{H} = 0.5$.

4.1.2 Unsteady Laminar Pipe Flow Results

Next, we use the unsteady, laminar pipe flow to validate the $D3Q27$ model in the presence of a curved wall. The Reynolds number (Re) based on the maximum center line velocity attained by the flow and the radius of the pipe is 20. The flow begins from rest and is simulated until it reaches steady state. Again, the flow is trigerred by the pressure difference at the two ends of the channel and the external body force term F_y according to the steady-state solution is

$$F_y = \frac{4\rho_0 \nu V_{max}}{R^2} \tag{4.5}$$

where V_{max} is the maximum velocity at the center of the pipe, ν is the kinematic viscosity and R is the pipe radius. Since the flow is laminar, there is no variation in the streamwise and the azimuthal directions. We need to resolve the flow in the radial direction. Hence, the length of the pipe can be set comparatively smaller than the radius of the pipe. The radius of the pipe is taken to be $R = 45\Delta x$, where Δx is the size of the grid-spacing. For the simulation, apart from the nodes corresponding to the fluid medium, we need two extra layers of nodes:

1. As buffer layers to be used after streaming.

Hence, the value of N_x, N_z should be greater than $2R + 2$. Hence, the computational domain size for this case is set to $N_x \times N_y \times N_z = 95 \times 8 \times 95$. The interpolated bounce back scheme is applied to fulfill the no-slip boundary condition. At the boundary node, the outward post-streaming distribution is related to the inward pre-streaming distributions by the quadratic interpolation scheme as explained in Sec. 3.3.1. We apply periodic boundary conditions in the streamwise direction. In the code, y represents the streamwise direction and x, z are the directions along $\theta = 0, 90$ respectively. The maximum streamwise velocity V_{max} is set to 0.05 and the speed of sound c_s is 0.5773. Hence, the maximum Mach number is much smaller than 1/3. The kinematic shear viscosity is calculated by using the definition of the Reynolds number

$$\nu = \frac{2V_{max}R}{Re}, \tag{4.6}$$

The relaxation parameters introduced in Sec. 3.1 are then given by the relation

$$\mathbf{s} = \frac{1}{3\nu + 0.5}, \tag{4.7}$$

The results obtained from the simulation are then compared with the analytical results obtained from solving the Navier-Stokes equation. For a laminar pipe flow, the Navier-Stokes equation reduces to a PDE where the velocity field is a function of the time and distance from the pipe center. The PDE is solved using separation of variables and the result mentioned in [38], is given by:

$$u_{theory} = 1 - \left(\frac{r}{R}\right)^2 - \sum_{n=1}^{\infty} \frac{8J_0(\lambda_n r/R)}{\lambda_n^3 J_1(\lambda_n)} exp\left(-\frac{\lambda_n^2 \nu t}{R^2}\right) \tag{4.8}$$

where J_0 and J_1 are Bessel functions of the zeroth and first order, respectively. t is the number of the time step, r represents the distance of the specified point from the center. λ_n is the n^{th} root of the Bessel function, otherwise known as the zero of Bessel function. In the simulation, it is impossible to sum infinite terms to get the theoretical solution of velocity. Therefore, only the first 10 terms are summed to get the analytical result at a certain time and position.

In Fig. 4.3, the time evolution of the streamwise velocity close to the pipe center has been plotted. The theoretical velocity at this location is also plotted as the

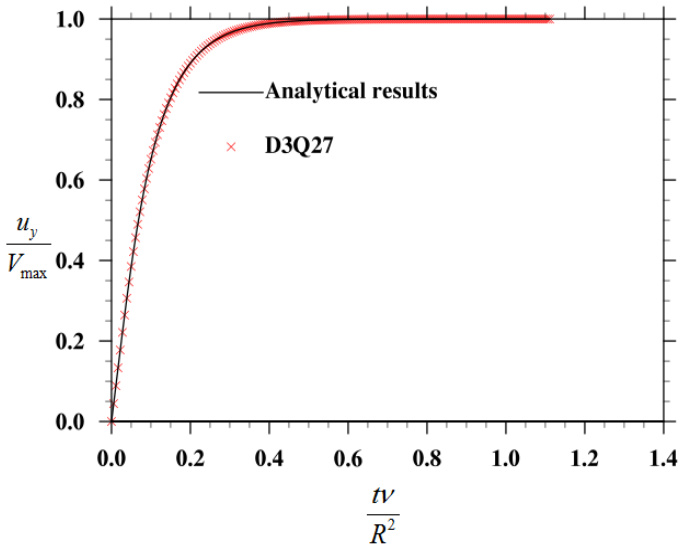

Figure 4.3: Time evolution of the streamwise velocity at $r = 0$(the pipe center). All the values are normalized as indicated.

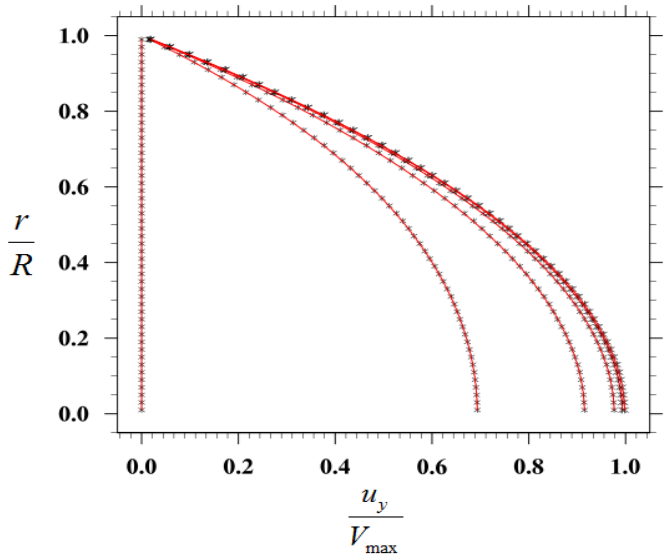

Figure 4.4: Streamwise velocity profiles at six different times, $t\nu/R^2 = 0$, 0.222, 0.444, 0.666, 0.888 and 1.111. All the values are normalized as indicated.

benchmark. We can see that the value of the streamwise velocity close to the pipe centerline steadily increases from 0 to 1 under the application of a constant uniform external force. The steady-state velocity is reached at roughly $\frac{t\nu}{R^2} = 0.5$ (see Fig. 4.3), similar to the case of laminar channel flow (see Fig. 4.1). In Fig 4.3, we see good agreement between the simulation results and the benchmark.

In Fig. 4.4, we plot the profiles of the streamwise velocity $\frac{v}{V_{max}}$ at different times $t\nu/R^2 = 0$, 0.222, 0.444, 0.666, 0.888 and 1.111. We also plot the analytical results at the given times as the benchmark. From Fig. 4.2, we can see excellent agreement between the analytical and the simulation results. The flow starts from rest and has already reached the steady state at $t\nu/H^2 = 1.111$. This can be deduced from the fact that the maximum value of the streamwise velocity is equal to one at the position $\frac{x}{R}$ = 1.0.

4.2 Effect of 3-D Lattice Models on the Simulation Results of Laminar Pipe Flows

In this section, we compare the results obtained from laminar pipe-flow simulations using two different 3D models: D3Q19 and D3Q27. We choose these two lattices over the D3Q15 lattice as they produce more accurate and stable results [30] and the availability of better computational resources has enabled us to employ these two models despite the increase in computational cost. The D3Q19 model used for the laminar-pipe flow simulations has been adopted from [37]. The D3Q27 model which we have used to simulate laminar-pipe flow has been derived in Sections. (3.1 and 3.2). To evaluate the accuracy of the two models we use L1 and L2-error norms:

$$L1 - error \equiv \frac{1}{n} \sum_{i=1}^{i=n} |u_{num,i} - u_{theory,i}| \tag{4.9a}$$

$$L2 - error \equiv \sqrt{\frac{\sum_{i=1}^{i=n} \left(u_{num,i} - u_{theory,i}\right)^2}{n}} \tag{4.9b}$$

Table 4.1: L1-norm for streamwise flow at different time steps.

Time Step	D3Q19	D3Q27
1000	5.22e-04	1.04e-04
2000	6.16e-04	1.22e-04
3000	6.51e-04	1.47e-04
4000	6.61e-04	1.64e-04
5000	6.62e-04	1.74e-04
6000	6.60e-04	1.79e-04
7000	6.57e-04	1.82e-04
8000	6.55e-04	1.83e-04
9000	6.53e-04	1.84e-04
10000	6.52e-04	1.84e-04

where n is the number of points and $u_{num,i}$, $u_{theory,i}$ are the numerical and theoretical values of the stream wise velocity at a particular point, normalized with the maximum centerline velocity.

Table 4.2: L2-norm for streamwise flow at different time steps.

Time Step	D3Q19	D3Q27
1000	5.15e-04	1.25e-04
2000	5.95e-04	1.46e-04
3000	6.30e-04	1.76e-04
4000	6.42e-04	1.96e-04
5000	6.44e-04	2.07e-04
6000	6.43e-04	2.13e-04
7000	6.41e-04	2.16e-04
8000	6.40e-04	2.18e-04
9000	6.38e-04	2.19e-04
10000	6.37e-04	2.19e-04

In Tables 4.1 and 4.2, we compare the L1 and L2-error norms calculated for the streamwise velocity at different time steps, and observe that the D3Q27 model produces more accurate results while simulating laminar pipe flow. We now perform the same error analysis for the secondary velocities in the radial and azimuthal directions.

Theoretically, both u_r and u_θ in a laminar pipe flow are non-existent. Hence, equations (4.9a) and (4.9b) become

$$L1 - error \equiv \frac{1}{n} \sum_{i=1}^{i=n} |u_{num,i}| \tag{4.10a}$$

$$L2 - error \equiv \sqrt{\frac{\sum_{i=1}^{i=n} u_{num,i}^2}{n}} \tag{4.10b}$$

Table 4.3: L1-norm for radial and azimuthal velocities at different time steps.

Time Step	u_r(D3Q19)	u_r(D3Q27)	u_θ(D3Q19)	u_θ(D3Q27)
1000	8.35e-06	4.84e-19	1.14e-04	5.50e-18
2000	1.12e-05	6.59e-19	1.51e-04	7.67e-18
3000	1.26e-05	8.19e-19	1.69e-04	9.19e-18
4000	1.34e-05	8.71e-19	1.79e-04	1.01e-17
5000	1.37e-05	9.07e-19	1.84e-04	1.05e-17
6000	1.39e-05	9.51e-19	1.87e-04	1.04e-17
7000	1.40e-05	9.36e-19	1.88e-04	1.05e-17
8000	1.41e-05	9.37e-19	1.89e-04	1.05e-17
9000	1.41e-05	9.23e-19	1.89e-04	1.08e-17
10000	1.41e-05	9.36e-19	1.89e-04	1.09e-17

From Tables. 4.3 and 4.4, we notice that the error-norms for the $D3Q19$ model are many orders of magnitude higher than that of the $D3Q27$ model. The error norms for u_r are an order of magnitude lesser than u_y and the error norms for u_θ are of the same order as u_y for the $D3Q19$ model. However, for the case of a $D3Q27$ model, the order of error-norms for u_r is one order less than the order of truncation error for a double precision number and the order of L1, L2 norms for u_θ are of the same order as that of the truncation error for a double precision number. Let us try to visualize the secondary flows for both the models and try to gain a deeper understanding of the source of the error for the case of a $D3Q19$ model.

In Fig. 4.5, we visualize the cross-flow vector fields for a laminar pipe flow after it reaches a steady state. The same scaling factor has been used for the two plots and

Table 4.4: L2-norm for radial and azimuthal velocities at different time steps.

Time Step	u_r(D3Q19)	u_r(D3Q27)	u_θ(D3Q19)	u_θ(D3Q27)
1000	1.17e-05	6.91e-19	1.95e-04	7.83e-18
2000	1.58e-05	9.47e-19	2.61e-04	1.11e-17
3000	1.78e-05	1.19e-18	2.94e-04	1.34e-17
4000	1.90e-05	1.27e-18	3.11e-04	1.48e-17
5000	1.96e-05	1.33e-18	3.21e-04	1.54e-17
6000	1.99e-05	1.38e-18	3.26e-04	1.52e-17
7000	2.01e-05	1.35e-18	3.29e-04	1.52e-17
8000	2.02e-05	1.37e-18	3.31e-04	1.53e-17
9000	2.02e-05	1.35e-18	3.32e-04	1.60e-17
10000	2.031e-05	1.36e-18	3.32e-04	1.60e-17

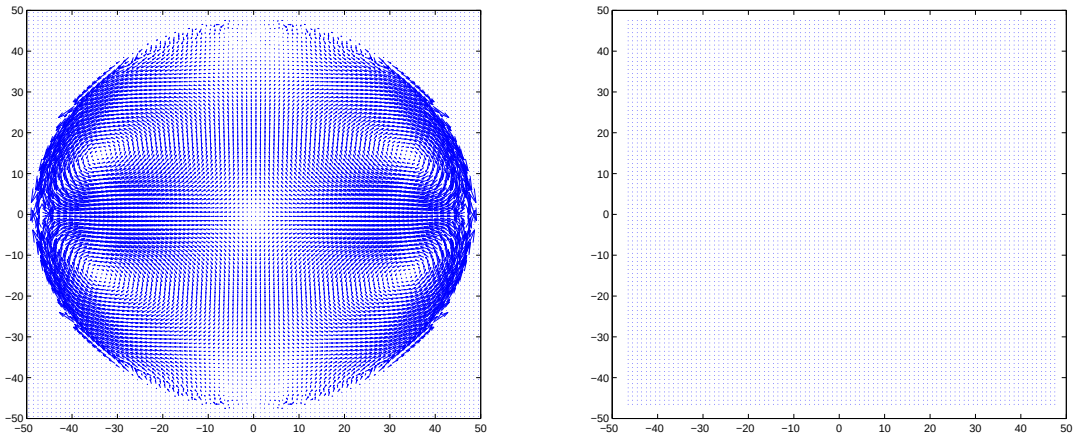

(a) D3Q19 model

(b) D3Q27 model

Figure 4.5: Mean cross-flow vector fields for the laminar pipe flow at time $t^* = 1.111$.

is equal to 5×10^{-4}/unit length. By comparing the vector plots for the two models, we notice that the $D3Q19$ model produces a strong secondary flow, especially, near the wall. However, for the $D3Q27$ model, the secondary flow is just noise produced due to the truncation of a double-precision floating-point number. In Fig. 4.5, we can clearly see that the secondary flow can be construed as four vortices whose centers are on diametrically opposite sides of the pipe. Fig.4.5 is a visual verification of Tables. 4.3 and 4.4, and we can conclude that using a $D3Q19$ model to simulate a laminar pipe flow produces a weak secondary flow consisting of four vortices as opposed to the $D3Q27$ model where the nonphysical secondary flow is not present.

4.3 Order of Accuracy for both the Models

Using the Chapman-Enskog analysis we can prove that the lattice Boltzmann method recovers, both continuity and Navier-Stokes equations with second-order accuracy [30]. The order of accuracy for the $D3Q19$ and the $D3Q27$ model can be determined by using the L1 and L2 error-norms for the laminar pipe flow. The error-norms are calculated for the streamwise velocity at time, $t^* = 1.111$ i.e. after the laminar pipe flow attains a steady state. To study the order of accuracy for laminar pipe flow, we choose four different pipe radii: $R = 10\Delta x, 15\Delta x, 30\Delta x$ and $45\Delta x$, where Δx is the grid-spacing. The order of accuracy n can now be estimated as

$$n(t) = log_{\left(\frac{r2}{r1}\right)}\left(\frac{\epsilon_{r1}(t)}{\epsilon_{r2}(t)}\right) \tag{4.11}$$

where ϵ_{r1} is the L1, L2 error-norm when the radius of the pipe is r1 and ϵ_{r2} is the L1, L2 error-norm when the radius of the pipe is r2. Graphically, the order of accuracy is equal to the slope of the logarithm of the L1 error-norm or the L2 error-norm vs the logarithm of radius of the pipe. Fig. 4.6 gives a summary of the results pertaining to the order of accuracy. These results are discussed in more detail in the next section.

4.4 Turbulent Pipe Flow Results

The final test case is the turbulent pipe flow which is a wall-bounded turbulent flow. As indicated in Sec. 1.1, no previous attempt has been made to perform direct

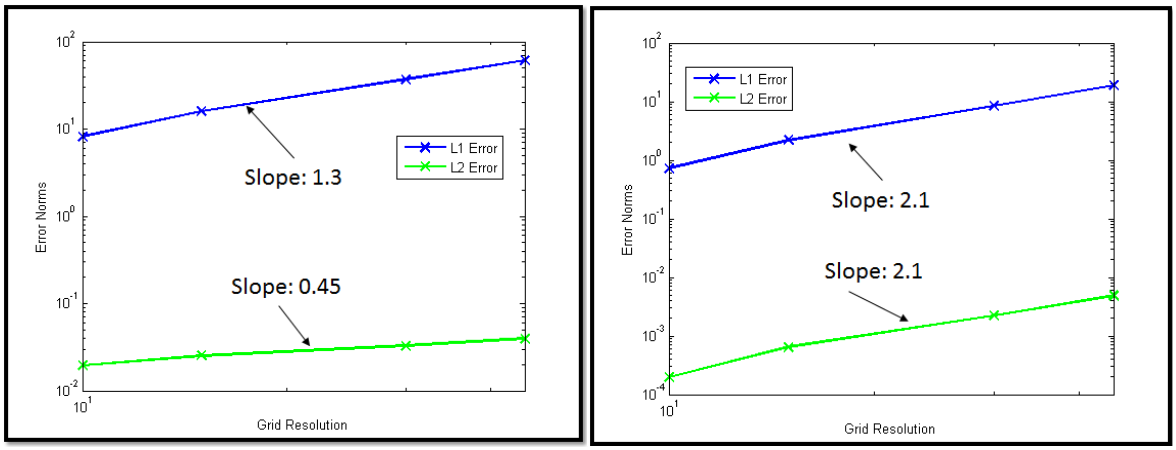

(a) D3Q19 model (b) D3Q27 model

Figure 4.6: Log plots of error norms with respect to the pipe radius (grid resolution) at time, $t^* = 1.111$. The order of accuracy is equal to the negative slope of the curve.

numerical simulation of turbulent pipe flow using LBM. The flow is locally inhomogenous and anisotropic, especially in the near-wall region. In this section, we study fully developed turbulent pipe flow of Reynolds number based on the friction velocity and the radius of the pipe, equal to 180. The friction velocity of the pipe is defined as $u_\tau = \sqrt{\tau_w/\rho}$. The dimensions of the pipe shown in Fig. 4.6 are $D \times D \times 2D$, where D is the diameter of the pipe. The domain size is equal to $300 \times 599 \times 300$. The kinematic shear viscosity is set to 0.032 and the relaxation parameters are related to the kinematic shear viscosity by the following relation:

$$\mathbf{s} = \frac{1}{3\nu + 0.5} \tag{4.12}$$

The velocity of the fluid is maintained such that the Mach number is much smaller than 1/3. The velocity is initialized by the "Law of the wall", which is given by the following equation:

$$u^+ = \begin{cases} r^+, \ r^+ < 10.8; \\ \frac{log(r^+)}{0.4} + 5.5, \ r^+ > 10.8 \end{cases}$$

where u^+ ($u^+ = \frac{u}{u_\tau}$) is the non-dimensionalized form of velocity and r^+ ($r^+ = \frac{(R-r)\times u_\tau}{\nu}$) is the wall coordinate. The friction velocity is calculated from the definition of Reynolds

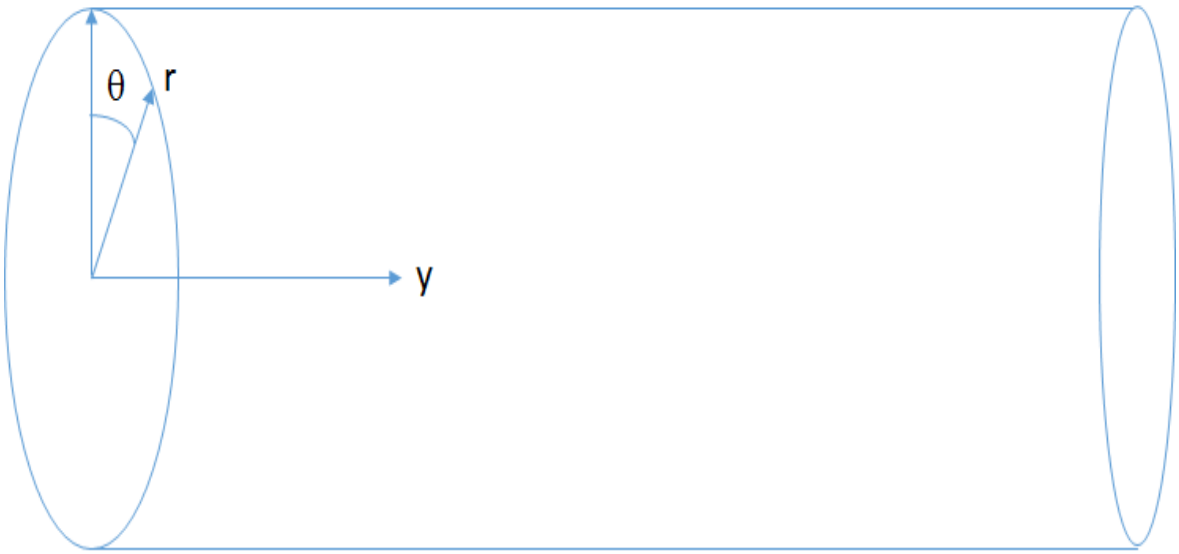

Figure 4.7: Flow geometry for turbulent pipe flow simulations

number i.e. $u_\tau = \frac{2Re\ \nu}{D}$. A constant body force F_y is applied to the streamwise direction and is equal to:

$$F_y = \frac{4\rho u_\tau^2}{D} \tag{4.13}$$

where u_τ is the friction velocity. Along with the constant body force, we apply, what is called a perturbation force to excite the flow for quick transition to a turbulent flow.

$$f_y = f_0 B_0 \frac{R}{r} sin\left(\frac{2\pi t}{T}\right) sin\left(\frac{2\pi(R-r-l_0)}{l}\right) sin\left(k_y \frac{2\pi y}{L_y}\right) cos(k_\theta \theta) \tag{4.14a}$$

$$f_r = -f_0 \alpha B_0 \frac{R}{r} \frac{k_y l}{L_y} sin\left(\frac{2\pi t}{T}\right) cos\left(\frac{2\pi(R-r-l_0)}{l}\right) cos\left(k_y \frac{2\pi y}{L_y}\right) cos(k_\theta \theta) \tag{4.14b}$$

$$f_\theta = f_0(\alpha) B_0 \frac{k_y}{k_\theta} \frac{2\pi R}{L_y} sin\left(\frac{2\pi t}{T}\right) sin\left(\frac{2\pi(R-r-l_0)}{l}\right) cos\left(k_y \frac{2\pi y}{L_y}\right) sin(k_\theta \theta) \tag{4.14c}$$

where k_y, k_θ are two frequencies of the perturbation force, T is the forcing period, B_0 is the forcing magnitude , α is the weighting parameter that distributes perturbation in radial and azimuthal direction and l_0, l define the forcing region in the radial direction. The two main principles to be observed behind designing such a force are:

1. The perturbation force recovers the constant physical body force when averaged over the whole domain.

2. The force satisfies the divergence free condition in cylindrical coordinate at every point of the flow domain

$$\bigtriangledown \cdot \overrightarrow{f} = \frac{1}{r}\delta_r(rf_r) + \frac{1}{r}\delta_\theta(f_\theta) + \delta_y(f_y) = 0 \tag{4.15}$$

The boundary condition used to simulate behavior at a solid-fluid interface is given by Yu et al.'s linear interpolation technique, as discussed in Sec. 3.3.1. We use periodic boundary conditions along the directions parallel to the flow. Let us look at how the value of the mean flow develops with time:

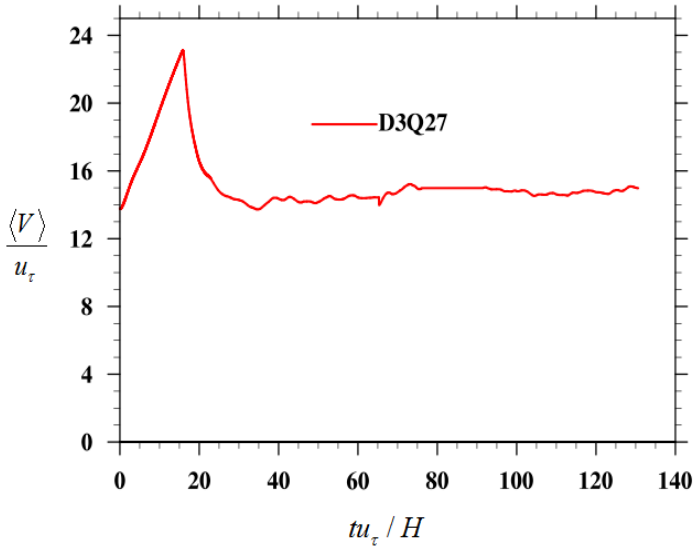

Figure 4.8: Time evolution of the streamwise velocity averaged over the whole domain. All the values are normalized as indicated.

From, the above figure, we can divide the simulation into three stages:

1. Pre-transition stage: Starting from the initial flow, the application of the perturbation force adds energy to the flow, but no obvious rapid transition of the energy from the mean flow to the velocity fluctuations. During this period, the mean velocity rises monotonically until the transition stage.

Table 4.5: Reference data

Reference	Scheme	Reynolds Number	Resolution (r $\times\theta\times$ z)	Pipe length
Loulou et al. [39]	Spectral	190	$72 \times 160 \times 192$	5D
Wagner et al. [40]	Finite volume	180	$70 \times 240 \times 486$	5D

2. Transition to turbulence: When the mean flow reaches to a high level, the flow became unstable with rapid transition of energy from the mean motion to the turbulent fluctuations. This period is represented by the decrease in the mean flow velocity.

3. Fully developed turbulent pipe flow: At this stage, the flow is statistically steady, though the instantaneous flow continues to change with time. At this stage, flow statistics can be averaged over a long time to obtain the mean and RMS velocity profiles. Similarly, higher order turbulence statistics such as Reynolds stress, skewness, etc can be computed.

To obtain the turbulence statistics, we average over approximately 40 eddy turnover times to compute the mean and the RMS velocity profiles. The details of the benchmark data to be compared with are mentioned in Table 4.5:

In the figures below, we compare the mean and RMS velocity profiles of fully developed turbulent pipe flow simulations using $D3Q19$ and $D3Q27$ models with the benchmark data.

Next, we compare the second-order turbulence statistics for the $D3Q19$ and $D3Q27$ model with the benchmark. The corresponding profiles of the Reynolds shear stress $- < u_y^{'} u_r^{'} / u_\tau^2 >$ are plotted in Fig. 4.11. Finally, in Fig. 4.12, we look at the contour plots of streamwise velocity averaged over the transverse sections of the pipe and time. To plot the contours, the streamwise velocity has been averaged over approximately 40 eddy turnover times.

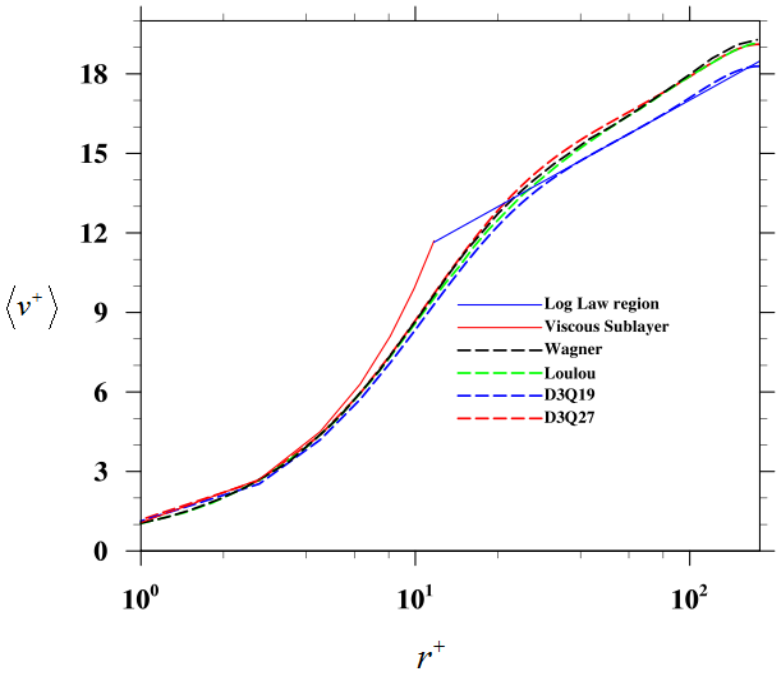

Figure 4.9: Profiles of mean streamwise velocity as a function of r^+ when the flow reaches the stationary stage. All the values are normalized as indicated.

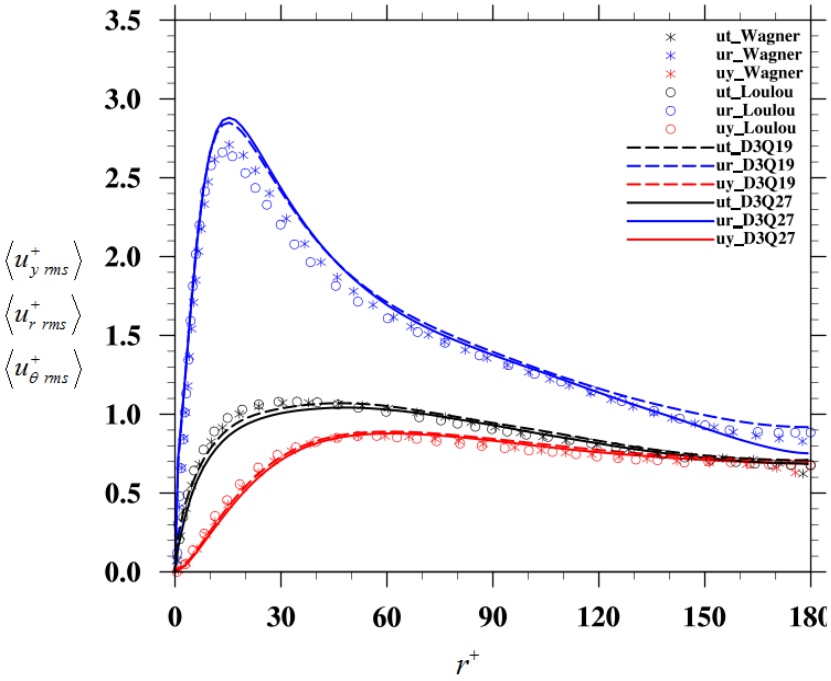

Figure 4.10: Profiles of RMS fluctuation velocities as a function of r^+ when the flow reaches the stationary stage. All the values are normalized as indicated.

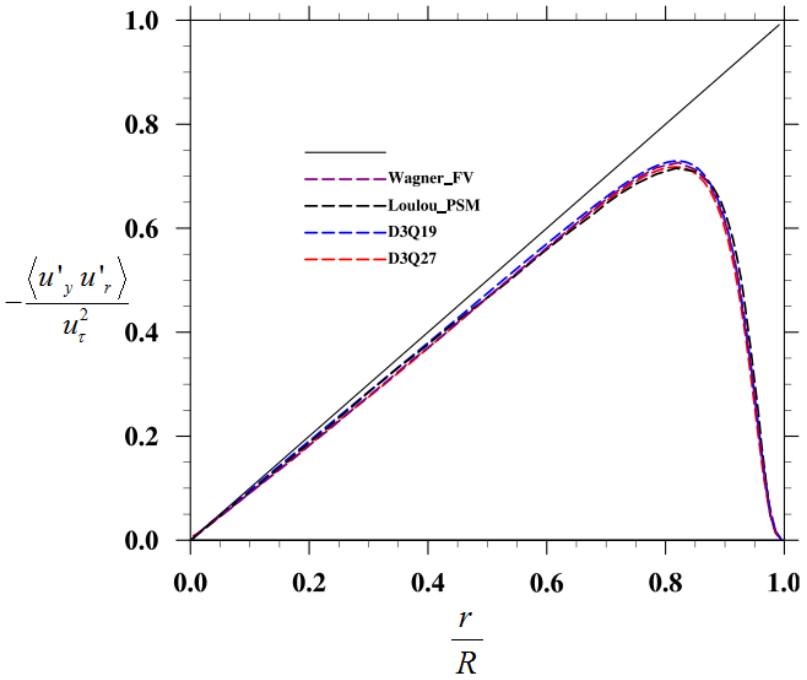

Figure 4.11: Profiles of average Reynolds stress as a function of r^+ when the flow reaches the stationary stage. All the values are normalized as indicated.

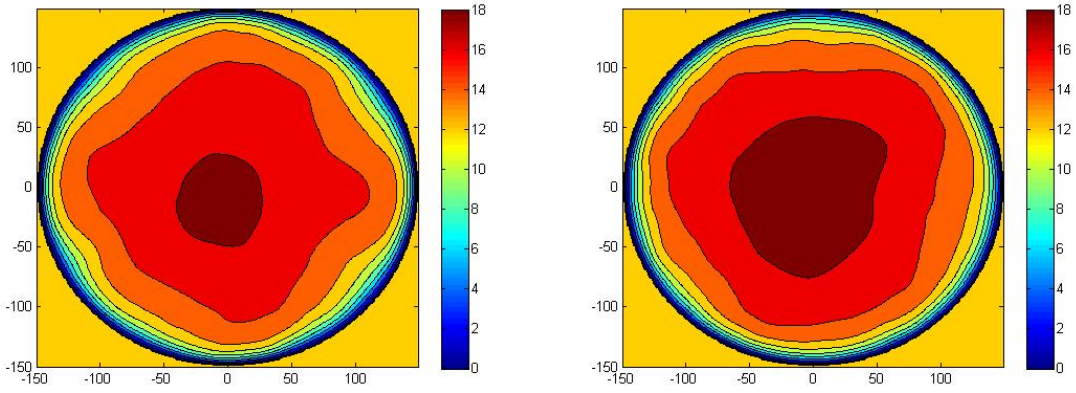

(a) D3Q19 model

(b) D3Q27 model

Figure 4.12: Mean stream wise velocity contour plot for fully developed turbulent pipe-flow

4.4.1 Relation between the Friction Reynolds Number and the Bulk Reynolds Number

The two major velocity scales taken into consideration while calculating the Reynolds number for laminar pipe flow are the friction velocity and the maximum velocity at the centerline. In this section, we derive the relation between the friction Reynolds number and the Reynolds number based on the maximum centerline velocity for a steady state laminar pipe flow. The streamwise velocity profile for a steady state laminar flow is given by the equation

$$\frac{u}{u_{cl}} = 1 - \left(\frac{r}{R}\right)^2, \tag{4.16}$$

The shear stress at the wall is then derived by using the Newton's law of viscosity i.e.

$$\tau = -\mu \frac{\partial u}{\partial r}, \tag{4.17}$$

where μ is the dynamic viscosity. From Eqs. (4.16) and (4.17), we have

$$\tau = \frac{2\mu u_{cl}}{R}, \tag{4.18}$$

The friction velocity is given by the relation

$$u_\tau = \sqrt{\frac{\tau}{\rho}} = \sqrt{\frac{2\mu u_{cl}}{\rho R}} = \sqrt{\frac{2\nu u_{cl}}{R}}, \tag{4.19}$$

where ν is the kinematic viscosity. Hence, according to the definition of the Reynolds number, we have

$$Re_\tau = \frac{2u_\tau R}{\nu} = \frac{2}{\nu}\sqrt{\frac{2\nu u_{cl}}{R}}R = 2\sqrt{\frac{2u_{cl}R}{\nu}}, \tag{4.20}$$

However, $\frac{2u_{cl}R}{\nu} = Re_{cl}$, where Re_{cl} is the Reynolds number based on the maximum centerline velocity. Hence, Eq. (4.20) reduces to

$$Re_\tau = 2\sqrt{Re_{cl}} \tag{4.21}$$

4.5 Timing Comparison of the $D3Q27$ Model with the $D3Q19$ Model

The wall clock index used to compare the execution speed of the codes incorporating the $D3Q19$ and $D3Q27$ models is given by the equation

$$WCI = \frac{W}{N_t} \times \frac{N_p}{N_x \times N_y \times N_z} \tag{4.22}$$

where W is the wall clock time taken to run the simulation, N_t is the number of time steps for which the simulation has been run, N_p is the number of processors used to run the simulation and $N_x \times N_y \times N_z$ is the resolution of the domain being simulated. In Table 4.6, we provide the details used for the calculation of the wall clock indices's for the two models:

Table 4.6: Calculation of wall clock indices's for the two models

	$D3Q19$	$D3Q27$
Wall clock time (seconds)	587	713
N_t	10000	10000
N_p	450	450
$N_x \times N_y \times N_z$	$300 \times 599 \times 300$	$300 \times 599 \times 300$
WCI	4.90E-07	5.95E-07

Chapter 5

CONCLUSIONS AND FUTURE SCOPE

In this chapter, we summarize the results of the study to arrive at some conclusions regarding the performance of the $D3Q27$ MRT model in comparison to the $D3Q19$ model. The prospective path forward is stated by discussing the future directions of this study.

5.1 Discussion and Conclusions

In Sec. 4.1, we validate the $D3Q27$ model used for the study by simulating the following cases:

Table 5.1: Summary of the test cases used for model validation

Flow case	Reynolds Number	Dominant length scale
Laminar channel flow	20	40 (Half-channel width)
Laminar pipe flow	20	45 (Radius of the pipe)

We select the above mentioned cases for validation of our model due to the presence of analytical results for cross-verification. From Figs. 4.1, 4.2, 4.3, and 4.4 we find perfect agreement of the simulation results with the analytical results, and as a result, can affirm to the accuracy of the $D3Q27$ model.

After the validation of the numerical code written in FORTRAN and MPI, we compare the performance of the $D3Q27$ model with the $D3Q19$ model for laminar pipe flow simulations. From Tables. 4.1 and 4.2, we can observe that the $D3Q27$ performs more accurately compared to the $D3Q19$ model for velocity in the stream wise direction. One of the more interesting observations from this study is the presence of an unphysical secondary flow in the $D3Q19$ simulation. From Fig. 4.5, we clearly

notice the presence of four vortices's at diametrically opposite ends. Tables. 4.3 and 4.4, further corroborate to the presence of a secondary flow while simulating laminar pipe flow with the $D3Q19$ model. However, no secondary flow is manifested in the simulation of a laminar pipe flow with the $D3Q27$ model. This can be deduced from the order of the L1 and L2 error-norms calculated for the radial and tangential velocities. We finally look at the order of accuracy for the $D3Q19$ and $D3Q27$ models. From Fig. 4.6 (a), one can observe the discrepancy between the results obtained and theory for the $D3Q19$ model. The order of the $D3Q19$ model is observed to be 1.3 and 0.45, which is significantly different from the theoretical prediction of 2. This discrepancy can be explained by the error induced at the curved boundary. From the vector plots in Fig. 4.5, one can notice a strong manifestation of errors near the curved boundary for the $D3Q19$ model. For the $D3Q27$ model, this is of much lesser intensity which renders the $D3Q27$ model approximately second order accurate. However, the $D3Q19$ model is not second order accurate due to the reasons discussed above.

Table 5.2: Summary of the turbulent pipe flow results used for comparison

Case	Method	Reynolds Number	Length of the Pipe
Loulou et al. [39]	Spectral	190	5D
Wagner et al. [40]	Finite volume	180	5D
$D3Q27$	LBM	180	2D
$D3Q19$	LBM	180	2D

In Table 5.2, we summarize all cases of turbulent pipe flow for which the first and second-order turbulent statistics have been compared. Before discussing the results in Sec. 4, let us discuss the effects of pipe length on turbulence statistics.

In a letter to Physics of Fluids, Chin et al. discuss the influence of pipe length on turbulence statistics. They state that the influence of pipe length on lower order statistics (such as the mean velocity profile) is less significant as compared to the higher order statistics (such as the RMS velocity profiles). They also state that one of the artifacts of a short pipe length is a higher peak RMS velocity value in the streamwise direction. From Fig. 4.9, we can observe that the mean velocity profile for the $D3Q27$

simulation agrees well with the reference data. However, the $D3Q19$ simulation under predicts the mean velocity away from the pipe wall. The mean velocity profile obtained from the $D3Q27$ simulation also conforms to the observation made by Eggels et al., which states that the mean velocity profile fails to the conform to the law of the wall even at Reynolds numbers considerably above 3000. The under-prediction of stream wise velocity by the $D3Q19$ model, especially near the center can be attributed to the lack of velocity vectors in the stream wise direction for the $D3Q19$ lattice, as stated in White et al. (2011).

An increase in the peak streamwise RMS velocity for the $D3Q19$ and $D3Q27$ simulations was observed in Fig. 4.10. This can be construed as an artifact of the short pipe length. In Fig. 4.11, we can further see that the Reynolds stress profiles have good agreement with the reference data for both the models. Finally in Fig. 4.12, we observe that the contours of the stream wise velocity for the $D3Q19$ model show a certain preference along the planes H and V (see Sec. 2.5). However, for the $D3Q27$ model, we do not observe obvious preference along a particular direction. The values of the streamwise velocity along D1 and D2 are observed to be lower than the value of streamwise velocity along H and V planes for the $D3Q19$ simulation. This provides further evidence of the hypthesis stated in White et al., as the planes along which lower value of streamwise velocity are observed are defective planes (i.e. planes consisting of lattices which have 5 velocity vectors instead of 9). These defective planes do not transfer momentum efficiently compared to the planes with 9 velocity vectors and this results in lower values of streamwise flow averaged over the whole domain.

In Sec. 4.4, we compare the execution speed of the $D3Q19$ and $D3Q27$ models. From Table 4.6, we can see that the $D3Q27$ model requires 21% more CPU time than the $D3Q19$ model. The relative difference is in fact lower than the expected value of 42%. However, the $D3Q27$ model produced more accurate results for both laminar and turbulent pipe flow cases. The statistics of the mean streamwise velocity away from the pipe wall is predicted much better by the $D3Q27$ model. In addition, the $D3Q27$ model exhibits rotational invariance, as opposed to the $D3Q19$ model.

5.2 Future Directions

The initial motivation of this study was to develop a model which successfully simulates a fully developed turbulent flow with a curved boundary. In Chapter 3, we identify the important components of the model and derive the model using an "inverse analysis". In Chapter 4, the model has been validated by comparing the results obtained from the laminar channel and pipe flow simulations with the analytical results, and the turbulent first and second order statistics with the benchmark results. The performance of the $D3Q27$ model has also been compared with the $D3Q19$ model. The $D3Q19$ takes lesser CPU time, but it fails to properly reproduce the exact physics for the case of laminar and turbulent pipe flow. Having identified a valid model ($D3Q27$ MRT) used to simulate turbulent flows with a curved boundary, we can now apply this model in the following manner:

1. Further study is needed to understand and improve the numerical stability of the MRT model, especially the $D3Q27$ model. In [43], the influence of the free parameters of the MRT model on its numerical stability was analyzed. In the above reference, Lallemand & Luo use linear stability analysis to improve the stability of their LBM model. They linearize the lattice Boltzmann equation by expressing the distribution function as a mean term and a fluctuation term. This results in an eigen-value problem known as the dispersion equation. We could optimize the values of the free parameters by solving for the eigen-values of the dispersion equation. An alternate method of improving the stability of the model might be, using different implementations of boundary conditions. The effects of a boundary condition implementation on the numerical stability are not well understood.

2. We can further extend the functionality of the code incorporating the $D3Q27$ model, and use it to simulate particle-laden turbulent pipe flows. In Wang et al. (2016), the authors simulate particle-laden turbulent channel flow using particle-resolved simulations. We can employ a similar treament to study particle-laden turbulent pipe flow and explore the effects of particles on turbulence modulation. Such interface resolved simulations open up a host of opportunities for turbulent particle-laden flow research.

REFERENCES

[1] George, William K. *Lectures in Turbulence for the 21st Century*, 2013.

[2] Reynolds, Osborne "An Experimental Investigation of the Circumstances Which Determine Whether the Motion of Water Shall Be Direct or Sinuous and of the Law of Resistance in Parallel Channels." *Proc. R. Soc. Lond.*, 1883.

[3] Ferro, Marco "Experimental Study on Turbulent Pipe Flow." *Technical Report from Royal Institue of Technology, Sweden*, 2012

[4] Avila, K. et al. "The Onset of Turbulence in Pipe Flow." *Science*, 2011

[5] Nikuradse, Johann "Law of Flow in Pipes: Reprinted in English." *NACA Technical Memorandum 1292*, 1950.

[6] Moody, Lewis F. "Friction Factors for pipe flow." *Trans. ASME*, 1944.

[7] Laufer, John. "The Structure of Turbulence in Fully Developed Pipe Flow." *NACA Report 1174*, 1954.

[8] Lundgren, T.S. "Turbulent Pipe and Channel Flow." *Physics of Fluids*, 1971.

[9] Tu, S.W. and Ramaprian, B.R. "Fully Developed Periodic Turbulent Pipe Flow: Part 1 & Part 2." *J. Fluid Mech.*, 1983.

[10] Reich, G. and Beer, H. "Fluid Flow and Heat Transfer in an Axially Rotating Pipe- 1 & 2." *Int. J. Heat Mass Transfer*, 1989.

[11] Kim, J., Moin, P. & Moser, R. "Turbulence Statistics in Fully Developed Channel Flow at Low Reynolds Number." *J. Fluid Mech.*, 1987.

[12] Barenbaltt, G.I., Chorin, A.J. & Prostokishin, V.M. "Scaling Laws for Fully Developed Turbulent Flow in Pipes." *Appl. Mech. Rev*, 1997.

[13] Zagarola, Mark V. & Smits, Alexander J. "Mean-Flow Scaling of Turbulent Pipe Flow." *J. Fluid Mech.*, 1998.

[14] Xu, S. & Martin, M. P. "Assessment of Inflow Boundary Conditions for Compressible Turbulent Boundary Layers." *Physics of Fluids*, 2004.

[15] Peixinho, J. & Mullin, T. "Decay of Turbulence in Pipe Flow." *Physical Review Letters*, 2006.

[16] Bailey, S. C. C., Vallikivi, M., Hultmark, M. & Smits, A.J. "Estimating the Value of von Karman's Constant in Turbulent Pipe Flow." *J. Fluid Mech.*, 2014.

[17] Chin, C., Ng, H.C.H, Blackburn, H.M., Monty, J.P. & Ooi, A. "Turbulent Pipe Flow at $Re_\tau \approx 1000$: A Comparison of Wall-Resolved Large-Eddy Simulation, Direct Numerical Simulation and Hot-Wire Experiment." *Computers & Fluids*, 2015.

[18] Norton, Tomas & Sun, Da-Wen. "Computational Fluid Dynamics (CFD) - an Effective and Efficient Design and Analysis Tool for the Food Industry: A Review." *Trends in Food Science & Technology*, 2006.

[19] Bao, Y.B. & Meskas, Justin. "Lattice Boltzmann Method for Fluid Simulations." *Report: Courant Institute of Mathematical Sciences*, 2011.

[20] Kim, J., Moin, Parviz & Moser, Robert. "Turbulence Statistics in Fully Developed Channel Flow at Low Reynolds Number." *J. Fluid Mech.*, 1987.

[21] D'Humieres, D. et al. "Multiple-relaxation-time Lattice Boltzmann Models in Three Dimensions." *Philosophical Transactions of the Royal Society A*, 2002.

[22] Moeng, C.H. & Sullivan, Peter P. "Large-Eddy Simulation." *Encyclopedia of Atmospheric Sciences*, 2015.

[23] Mohamad, A.A. *Lattice Boltzmann Method: Fundamentals and Engineering Applications with Computer Codes*. Springer, 2011.

[24] Chen, Shiyi & Doolen, Gary D. "Lattice Boltzmann Method for Fluid Flows." *Annu. Rev. Fluid Mech.*, 1998.

[25] Bhatnagar, P.L., Gross, E.P. & Krook, M. "A Model for Collision Processes in Gases. 1. Small Amplitude Processes in Charged and Neutral One-Component Systems." *Phys. Rev.*, 1954.

[26] Lammers, P et al. "Lattice BGK Direct Numerical Simulation of Fully Developed Turbulence in Incompressible Plane Channel Flow." *Computers & Fluids*, 2006.

[27] Premnath, Kannan N., Pattison, Martin J. & Banerjee, Sanjoy. "Generalized Lattice Boltzmann Equation with Forcing Term for Computation of Wall-Bounded Turbulent Flows." *Physical Review E*, 2009.

[28] Bespalko, Dustin., Pollard, Andrew. & Uddin, Mesbah."Direct Numerical Simulation of Fully-Developed Turbulent Channel Flow Using the Lattice Boltzmann Method and Analysis of OpenMP Scalability." *High Performance Computing Systems and Applications Volume 5976: Lecture Notes in Computer Science.*, 2010.

[29] Freitas, R.K et al. "Analysis of Lattice-Boltzmann Methods for Internal Flows." *Computers & Fluids*, 2011.

[30] Kang, Shin K. & Hassan, Yassin A. "The Effect of Lattice Models Within the Lattice Boltzmann Method in the Simulation of Wall-Bounded Turbulent Flows." *Journal of Computational Physics*, 2013.

[31] White, A.T. & Chong, C.K. "Rotational Invariance in the Three-Dimensional Lattice Boltzmann Method is Dependent on the Choice of Lattice." *J. Comput. Phys.*, 2011.

[32] Suga, K et al. "A D3Q27 Multiple-Relaxation-Time Lattice Boltzmann Method for Turbulent Flows." *Computers and Mathematics with Applications*, 2015.

[33] Anupindi, K., Lai, Weichen. & Frankel, S. "Characterization of Oscillatory Instability in Lid Driven Cavity Flows Using Lattice Boltzmann Method." *Computers & Fluids*, 2013.

[34] Xu, H., Malaspinas, O. & Sagaut, P. "Sensitivity Analysis and Determination of Free Relaxation Parameters for the Weakly-Compressible MRT-LBM Schemes." *Journal of Computational Physics*, 2012.

[35] Peng, C. et al. "Implementation Issues and Benchmarking of Lattice Boltzmann Method of Moving Rigid Particle Simulations in a Viscous Flow." *Computer and Mathematics with Applications*, 2016

[36] Yu et al. "Viscous Flow Computation with the Method of Lattice Boltzmann Equation." *Prog. Aerospc. Sci.*, 2003.

[37] Wang, Lian-Ping et al. "Lattice Boltzmann Simulation of Particle-Laden Turbulent Channel Flow." *Computers and Fluids*, 2016.

[38] Wang, Lian-Ping, Du, Michael H. "Direct Simulation of Viscous Flow in a Wavy Pipe Using the Lattice Boltzmann Approach." *Int. J. Engineering Systems Modelling and Simulation*, 2008.

[39] Loulou, Patrick et al. "Direct Numerical Simulation of Incompressible Pipe Flow Using a B-Spline Spectral Method.",*NASA Technical Memorandum 110436*, 1997.

[40] Friedrich, R. et al. "Direct Numerical Simulation of Incompressible Turbulent Flows." *Computer & Fluids*, 2001.

[41] Chin, C. et al. "The Influence of Pipe Length on Turbulence Statistics Computed from Direct Numerical Simulation Data.",*Physics of Fluids*, 2010.

[42] Eggels, J.G.M. "Fully Developed Turbulent Pipe Flow: A Comparison Between Direct Numerical Simulation and Experiment." *Journal of Fluid Mechanics*, 1994.

[43] Lallemand, Pierre & Luo, "Theory of the Lattice Boltzmann Method: Dispersion, Dissipation, Isotropy, Galilean Invariance and Stability." *Physical Review E*, 2000.

[44] Wang, Lian-Ping et al. "Lattice Boltzmann Simulation of Particle-Laden Turbulent Channel Flow." *Computers and Fluids*, 2016.

Appendix A

CHAPMAN-ENSKOG ANALYSIS

The lattice Boltzmann equation with the multiple-relaxation-time collision model is expressed as:

$$f_i(\mathbf{x}+\mathbf{e}_i\delta_t, t+\delta_t) - f_i(\mathbf{x},t) = -\mathbf{M}^{-1}\mathbf{S}\left[\mathbf{m}(\mathbf{x},t) - \mathbf{m}^{eq}(\mathbf{x},t)\right] + \Phi_i \tag{A.1}$$

where f_i is the distribution function associated with the molecular velocity $\mathbf{e}_i$, $\mathbf{x}$ and t are spatial and time coordinates, respectively. The first term on the right hand side of Eq. (A.1) describes the MRT collision operator and the second term $\Phi_i[kg\cdot m^{-3}]$ is used to represent the mesoscopic forcing term which accounts for the effect of macroscopic forcing $\mathbf{F} \equiv (F_x, F_y, F_z)[kg\cdot m^{-2}\cdot s^{-2}]$. After multiplying Eq. (A.1) by $\mathbf{M}/\delta_t$, we obtain

$$\left(\mathbf{I}\partial_t + \hat{\mathbf{C}}_\alpha\nabla_\alpha\right)\mathbf{m} + \frac{\delta_t}{2}\left(\mathbf{I}\partial t + \hat{\mathbf{C}}_\alpha\nabla_\alpha\right)^2\mathbf{m} = -\frac{\mathbf{S}}{\delta_t}\left(\mathbf{m}-\mathbf{m}^{(eq)}\right) + \mathbf{\Psi} \tag{A.2}$$

where $\mathbf{I}$ is an identity matrix, $\mathbf{\Psi} \equiv \mathbf{M}\mathbf{\Phi}/\delta_t$ denote the moments associated with the forcing term, ∂_t stands for the time derivative, ∇_α with $\alpha = x$, y, or z denotes the spatial derivatives and $\hat{\mathbf{C}}_\alpha \equiv \mathbf{M}diag(e_{1\alpha})\mathbf{M}^{-1}$. The following multiscale expansion is then applied to $\mathbf{m}$, $\mathbf{m}^{(eq)}$, ∂_t, ∇_α, and $\mathbf{\Psi}$:

$$\mathbf{m} = \mathbf{m}^{(0)} + \epsilon\mathbf{m}^{(1)} + \epsilon^2\mathbf{m}^{(2)} + ... \tag{A.3a}$$

$$\mathbf{m}^{(eq)} = \mathbf{m}^{(eq,0)} + \epsilon\mathbf{m}^{(eq,1)} \tag{A.3b}$$

$$\partial_t = \epsilon\partial_{t1} + \epsilon^2\partial_{t2} \tag{A.3c}$$

$$\nabla_\alpha = \epsilon\nabla_{1\alpha} \tag{A.3d}$$

$$\mathbf{\Psi} = \epsilon \mathbf{\Psi}^{(1)} \tag{A.3e}$$

where ϵ is the Knudsen parameter, $t1$ is the fast (advection) time scale and $t2$ is the slow (diffusion) time scale. Substituting Eq. (A.3) into Eq. (A.2) and using perturbation analysis, we obtain the Chapman-Enskog equations:

$$O(1) : \mathbf{m}^{(0)} = \mathbf{m}^{(eq)}, \tag{A.4a}$$

$$O(\epsilon) : \left(\mathbf{I}\partial_{t1} + \hat{\mathbf{C}}_\alpha \partial_{1\alpha}\right)\mathbf{m}^{(0)} = -\frac{\mathbf{S}}{\delta_t}(\mathbf{m}^{(1)}) + \mathbf{\Psi}^{(1)}, \tag{A.4b}$$

$$O(\epsilon^2) : \partial_{t2}\mathbf{m}^{(0)} + \left(\mathbf{I}\partial_{t1} + \hat{\mathbf{C}}_\alpha \partial_{1\alpha}\right)\left[\left(1 - \frac{\mathbf{S}}{2}\right)\mathbf{m}^{(1)} + \frac{\delta_t}{2}\mathbf{\Psi}^{(1)}\right] = -\frac{\mathbf{S}}{\delta_t}\mathbf{m}^{(2)} \tag{A.4c}$$